Sedimentary Geology 436 (2022) 106158

Contents lists available at ScienceDirect

Sedimentary Geology

journal homepage: www.elsevier.com/locate/sedgeo

Coarse calcite grains in hydrocarbon-rich tuffaceous mudstone in a Permian volcanic lake—An indicator for subaqueous volcanic deposition and related hydrocarbon generation

Xin Jiao [a,*], Yiqun Liu [a], Wan Yang [b,*], Shuangshuang Wang [c], Ziyuan Meng [a], Zhexuan Li [a], Hong Li [a], Minru Zhao [a]

[a] State Key Laboratory of Continental Dynamics, Department of Geology, Northwest University, Xi'an 710069, Shaanxi, China
[b] Geology and Geophysics Program, Missouri University of Science and Technology, Rolla, MO 65409, USA
[c] Xi'an Center of China Geology Survey, Xi'an 710054, Shaanxi, China

article info

Article history:
Received 18 February 2022
Received in revised form 25 April 2022
Accepted 3 May 2022
Available online 07 May 2022

Editor: Dr. Catherine Chagué

Keywords:
Calcite grains
Fine-grained sedimentary rocks
Volcanic-hydrothermal activities
Subaqueous explosion
Hydrocarbon generation
Permian

abstract

Sediments originated from volcanic-hydrothermal activities show clear relationship with hydrocarbon generation and accumulation in fine-grained sedimentary rocks at a regional scale. However, the fundamental processes and mechanisms of this relationship are still poorly understood at a microscopic scale to hamper efficient hydrocarbon exploration. In addition, coarse grains common in volcanic lacustrine fine-grained sediments have been traditionally interpreted as diagenetic products during early and late burial. Our study, however, suggests that coarse calcite grains are not diagenetic, but formed by subaqueous explosion. The calcite grains occur in lacustrine fine-grained sedimentary rocks in the middle Permian Lucaogou Formation in the Santanghu intracontinental rift basin, NW China. They are sand sized, angular, mono- and polycrystalline, and discretely scatter in silt to clay-sized non-calcite pyroclastic matrix. The calcite grains and the mud matrix are interpreted as a pyroclastic debris flow deposit. In-situ $^{87}Sr/^{86}Sr$ ratios (0.704932–0.705840, and 0.705137 on average) of the calcite grains are similar to those of mantle rocks, indicating an origin closely related to mantle-derived fluids. The in-situ $\delta^{13}C$ values (4.24‰ to 5.06‰, and 4.57‰ on average) and extremly negative $\delta^{18}O$ values (−21.70‰ to −21.18‰, and − 21.49‰ on average) indicate that extensive hydrothermal alteration and microbial activities influenced the formation of the calcite. Element composition and homogenizaiton temperature of fluid incusions of calcite and biomarkers of the mudstone all suggest a relatively low-temperature hydrothermal condition in a saline and reducing environment. Furthermore, hydrocarbon-rich inclusions are rich in the calcite grains and have two modes of occurrence and maturity. They indicate that the organic matter was generated from algae bloom, which was caused by volcanic-hydrothermal activities. Alternatively, the hydrocarbon may have an inorganic origin originated from a mantle source. Our findings provide an alternative interpretation on the origin of coarse calcite grains in fine-grained sedimentary rocks and demonstrate a microscopic relationship between volcanic-hydrothermal activities and hydrocarbon generation and accumulation in a tectonic active rift basin.

1. Introduction

Over the past decades, it has been observed that materials originated from the deep earth, including fluids and minerals formed by volcanichydrothermal activities, have a close relationship with hydrocarbon generation and accumulation through organic-inorganic interaction (Weitze, 1985; Liu et al., 2019; Procesi et al., 2019; Jiao et al., 2020). Oil accumulations have been found in areas of volcanic-hydrothermal deposits within ~300 km from volcanic centers worldwide (Bigi et al., 2015; Berndt et al., 2016; Liu et al., 2019; Procesi et al., 2019). In addition, sediments from volcanic eruption and hydrothermal precipitation have been observed in many hydrocarbon source rocks in petroliferous basins (Weitze, 1985; Jiao et al., 2020). For example, the alkaline lakes influenced by volcanic-hydrothermal activities and evaporation have extremely high primary productivity, and their deposits serve as critical source rocks in some basins, such as the Paleogene Green River Formation in U.S.A., the Cambrian Observatory Hill Formation in Australia, and the Permian Fengcheng Formation in China (Cangemi et al., 2016; Cao et al., 2020; Guo et al., 2021). Furthermore, many lacustrine source rocks are hydrocarbon-rich fine-grained sedimentary rocks with volcanic-hydrothermal deposits in some Chinese petroliferous basins, such as Permian Lucaogou Formation in Santanghu and Junggar basins (Liu et al., 2012; Jiao et al., 2018a, 2018b, 2020), Cretaceous Tengger Formation in ErlianBasin (Yang et al., 2020, 2021b), Bayingebi Formation in Yin'e Basin (Zhang et al., 2020), Yingcheng Formation in Songliao Basin (Shan et al., 2013), and Xiagou Formation in Jiuquan Basin (Wen et al., 2013). The rocks are important unconventional oil and gas reservoirs amid the increasing demand for unconventional hydrocarbon resources (Zou et al., 2014; Liang et al., 2018; Jiang et al., 2021). These source rocks all formed in rift basins, suggesting direct influence and participation of mantle-originated materials in lacustrine sedimentation. However, these fine-grained rocks have commonly been misinterpreted as simple terrestrial sedimentary deposits for a long time, because the great difficulties in petrological and mineralogical studies of very fine-grained sediments (Jiao et al., 2020; Jiang et al., 2021).

Four effects of volcanic-hydrothermal activities on hydrocarbon generation, migration, and accumulation have been speculated (Liu et al., 2019). First, volcanic-hydrothermal activities produce abundant gas of CO_2, CH_4, H_2, and NH_3, and ions of Fe, Mn, Zn, Co, and Cu (Botz et al., 2002; Capaccioni et al., 2004; Shuai et al., 2018; Liu et al., 2019), many of which can serve as nutrients to increase organic productivity. Second, thermal energy released by volcanic-hydrothermal activities speed up the generation process from organic matters to hydrocarbon. Simoneit (1984) termed this petroleum as "hydrothermal petroleum" in the Guaymas Basin in the Gulf of California, and was observed in some other rift basins, such as the East African Rift Valley (Simoneit et al., 2000), Red Sea Trough (Michaelis et al., 1990), and Bohai Bay Basin (Zhu et al., 1994). Third, deep fluids upwelling through fractures dissolved some constituents in reservoir rocks to improve the porosity and permeability (Smith, 2006; Davies and Smith, 2006). Finally, deep supercritical CO_2 may displace retained oil in deep and tight reservoirs and CH_4 in shale to facilitate hydrocarbon migration (Hyatt, 1984; Liu et al., 2019). However, these speculations are based on modern observations. More researches on ancient examples are required.

Petrographically, sand and gravel-sized grains in fine-grained sedimentary rocks deposited in many environments are commonly sparse, but may indicate exceptionally sedimentary environments and processes (White and Houghton, 2006; de Silva et al., 2013; Benison, 2017, 2019; Łapcik et al., 2021). In volcanic-hydrothermallyinfluenced alkaline lakes, they are commonly interpreted as replacement from gypsum or alkaline minerals formed during evaporation (Garcia-Fresca et al., 2018; Cao et al., 2020; Guo et al., 2021). The possibility of those grains originated from subaqueous volcanic eruption is not well documented (White and Houghton, 2006). More detailed microscopic studies will improve our understanding of the effect of volcanic-hydrothermal activities on the origin of those grains so as to provide insights to aid in hydrocarbon exploration.

In this study, we characterize sand-sized mono- and polycrystalline calcite grains accumulated in hydrocarbon-rich mudstones in the middle Permian Lucaogou Formation in Santanghu Basin. The petrographic and geochemical characteristics of the grains and the hosted tuffaceous mudstone, and the underlying and overlying tuffaceous mudstones without calcite grains are compared. The sedimentary products and processes of subaqueous volcanic-hydrothermal activities and related hydrocarbon generation are discussed. This study provides an ancient analog for future research on the role of volcanichydrothermal activities on lacustrine sedimentation and hydrocarbon generation.

2. Geological background

The Santanghu Basin is a late Palaeozoic intracontinental rift basin located in the north of the Bogda Mountains in northwestern China (Fig. 1A). Two major tectonic episodes formed its basement during Carboniferous and a series of grabens, where fluvial-lacustrine sediments started to accumulate since the early Permian (Zhou et al., 2006; Xia et al., 2008; Yang et al., 2021a). The basin contains five sags, among which the Malang Sag is the target area for oil exploration and the focus of this study.

The Permian Lucaogou Formation is composed mainly of lacustrine fine-grained rocks with common carbonate rocks deposited in an intracontinental sediment-starved, deep, stratified, and anoxic lake (Liu et al., 2012). It is an important source rock and shale oil reservoir in the Santanghu Junggar, and Turpan-Hami basins in north Xinjiang (Li et al., 2015; Hackley et al., 2016; Liu et al., 2017; Zhang et al., 2018, 2020). It is sandwiched by two regional volcanic rock-dominated formations (Fig. 1B–E). The underlying lower Permian Kalagang Formation consists of intermediate-felsic igneous rocks and tuff, while the overlying middle Permian Tiaohu Formation consists mainly of mafic volcanic rocks and tuffaceous shale (Wang et al., 2015).

⁎ Corresponding authors.
E-mail addresses: jxin807@nwu.edu.cn (X. Jiao), yangwa@mst.edu (W. Yang).

https://doi.org/10.1016/j.sedgeo.2022.106158 0037-0738/

Laminated dolostone and tuffaceous shale intercalated with tuff are the main lithological association in the Lucaogou Formation (Jiao et al., 2020; Liu et al., 2020). However, the complex mineral composition and heterogeneity complicate the interpretation of the distribution of lithofacies and hydrocarbon accumulations. The results of conventional fracturing technique for the Lucaogou shale show fast production decline, low recovery, and poor economics (Liang et al., 2019; Xu et al., 2020). The Lucaogou Formation contains cone-shaped volcanichydrothermal build-ups on seismic section (Jiao et al., 2018a, 2018b). Fine sand to silt-sized angular alkaline feldspars, analcite, diopside, and shard-like vitric grains are common in laminated core samples with soft-sediment deformation, indicating high-density pyroclastic flow deposits (Jiao et al., 2018a). Silt to clay-sized pyroclastic grains and hydrothermally-originated carbonate and siliceous minerals occur in various lithofacies (Liu et al., 2012; Jiao et al., 2018b, 2020). Strikingly, those minerals show relationship with hydrocarbon accumulation. For example, the dolomite-bearing tuffaceous shale and tuffaceous dolostone have the highest total organic carbon (TOC) content and oil generation potential. In addition, some shales containing hydrothermally precipitated quartz and hydrothermally altered buddingtonite also have a high TOC content (Jiao et al., 2020; Pan et al., 2020; Liu et al., 2020; Zhang et al., 2021). Hence, the unique lithologies in the Lucaogou Formation make them good candidates to study subaqueous volcanic explosion, hydrothermal activities, and related hydrocarbon generation.

3. Data and methods

Five beds of mudstone containing sand-size calcite grains in the Lucaogou Formation were observed at the depth of 2320–2321 m in Well M10 in the Malang Sag in Santanghu Basin (Fig. 1A). The well is close to a field dominated with interpreted volcanic deposits (Fig. 1B– D). The Lucaogou in the well is mainly composed of well laminated dolomite-bearing tuffaceous shale with thin tuffaceous dolostones in the lower part and rare siltstones in the uppermost part (Fig. 1E), which indicate that pyroclastics and chemical precipitates are the dominant sediments in this area. A 5-cm core from the five mudstone beds was used in this study for its representative composition, texture, and structure. The core was cut into four pieces numbered as M10-A, M10-B, M10-C, and M10-D. The underlying (M10U) and overlying (M10O) segments of the core, which do not contain calcite grains, were used for comparative study. Sample M10-A was polished for observation of macroscopic sedimentary structures. Sample M10-B was made into a thin section for observation using polarizing microscope, microprobe, Tescan Integrated Mineral Analyzer (TIMA), and fluid inclusion analysis. Sample M10-C was prepared for strontium, carbon, and oxygen isotopes. Samples M10-D, M10O, and M10U were powdered for XRD, Rock Eval pyrolysis and biomarker analysis.

The micro-structures and textures of calcite grains and distribution of organic matter were first documented in thin section using polarizing and fluorescent microscope (OLYMPUS, U-LH100HG), then using the electron microprobe (JXA-8100, 15 KV, beam spot size 1 μm) for mineralogical and chemical confirmation and textures of silt to clay-sized

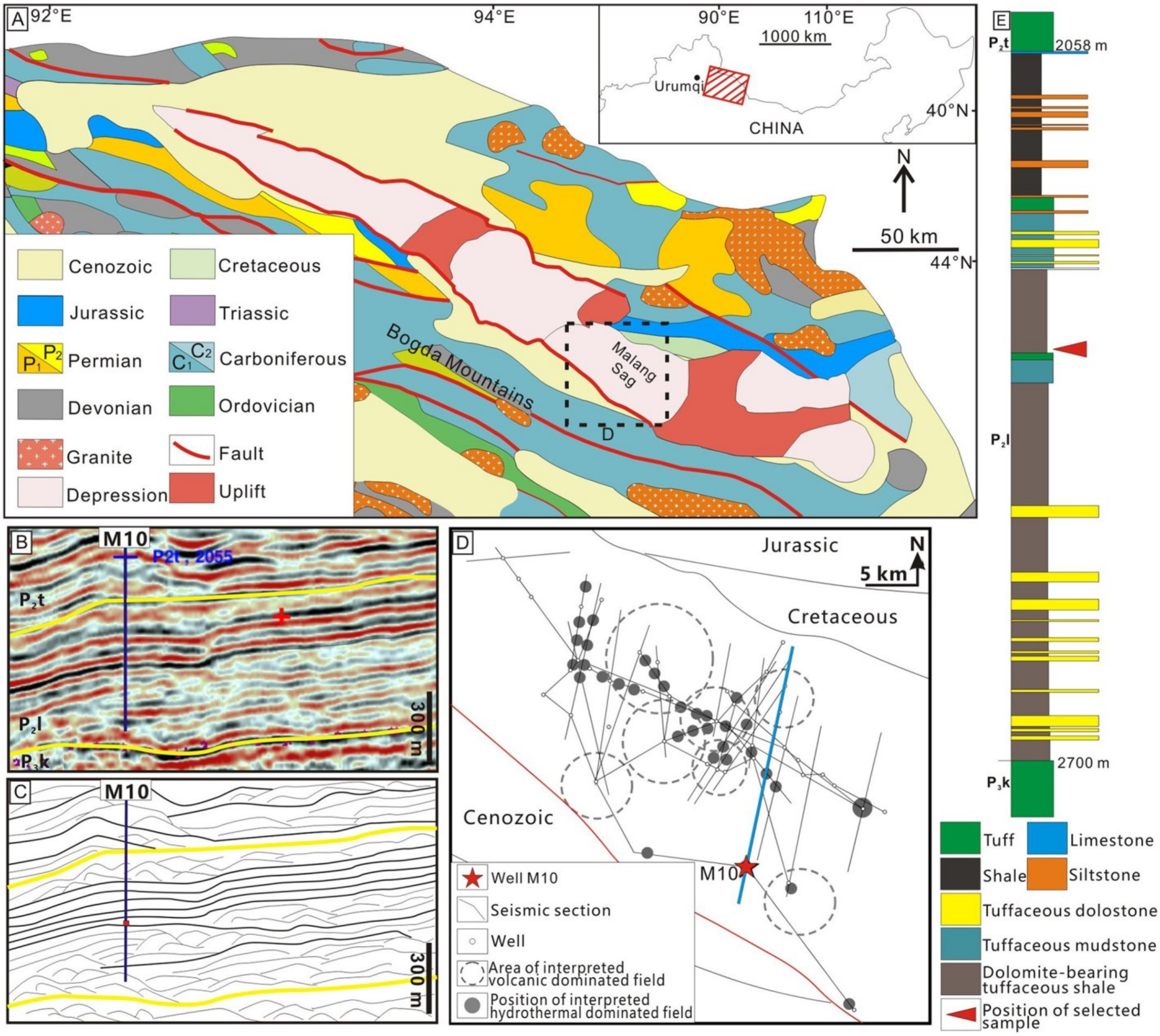

Fig.1. A. Simplified geological map of Santanghu Basin showing the surrounding outcrop areas, and sags and uplifts in the subsurface. Black dashed box is the location of (D). Modified after Ma et al. (2002). B. A 2-D seismic section close to the sampling well M10. Yellow lines are sequence boundaries. P_2t — middle Permian Tiaohu Formation; P_2l — middle Permian Lucaogou Formation; P_3k — lower Permian Kalagang Formation. C. Line drawings of (B) showing stratigraphic features. The seismic reflections in the lower and uppermost parts of the Lucaogou Formation on the seismic sections are discontinuous and chaotic with some cone-shaped stratigraphic buildups, whereas the middle part contains continuous high-amplitude reflections. The red box is the location of selected sample. D. Interpreted volcanic and hydrothermal fields in Malang Sag (modified after Jiao et al., 2018b). Blue line is the location of the seismic section of (B). E. Lithostratigraphy of Lucaogou Formation in Well M10. It is interpreted from well logs and partly core observations. (For interpretation of the references to color in this figure legend, the reader is referred to the web version of this article.)

grains. The mineralogy, volumetric percentage, and occurrence of various minerals were documented on the thin section using TIMA (beam energy 25,000 eV, probe current 8.85 nA, beam spot size 74 nm).

Geochemical analysis was conducted to obtain the strontium, carbon, and oxygen isotopes of the calcite grains to interpret the origin and controlling factors of the fluid that formed the calcite. A selected sample was split into two parts. One part was made into a thin section with a thickness of 60 μm for strontium isotope analysis, while the other part was crudely polished to form a flat surface. Twenty pristine sand-sized calcite grains, numbered as M-1 to M-20, were selected and their major element compositions were documented using the electron microprobe. In-situ analysis of strontium isotope and trace elements composition of the calcite grains was performed using a Geolas Pro laser-ablation system with a beam size of 44 μm, which is coupled to a Neptune multiple-collector ICP-MS in the Key Laboratory of Xi'an Center of the Chinese Geological Survey. Fifteen calcite grains were micro-drilled on the flat surface to obtain one sample of mixed powder for carbon-oxygen isotope analysis using a MAT252 mass spectrometer at the Laboratory of Continental Dynamics in Northwest University, China. A total of five such mixed samples, numbered as M10-C-1 to M10-C-5, were analyzed.

The morphology, distribution, and homogenization temperature of fluid inclusions in calcite grains were tested to obtain the fluid characteristics. About 100 inclusions were identified using microscope under plane-polarized light and fluorescence incident blue light. The primary and secondary of inclusions were differentiated on the basis of their distribution and morphology. 45 primary inclusions were selected for further analysis. The chemical compositions of 15 out of the 45 inclusions were obtained through micro-Raman spectroscopy. The other inclu- LINKAM THMS600 (−196–600 °C in testing range and ±1 °C in heating sions are filled mainly with hydrocarbons. The homogenization temper- error) in the Department of Geology, Northwest University, China. Fiature of the 15 inclusions was obtained using a cooling-heating stage nally, the microscopic fluorescence spectra of hydrocarbon-rich

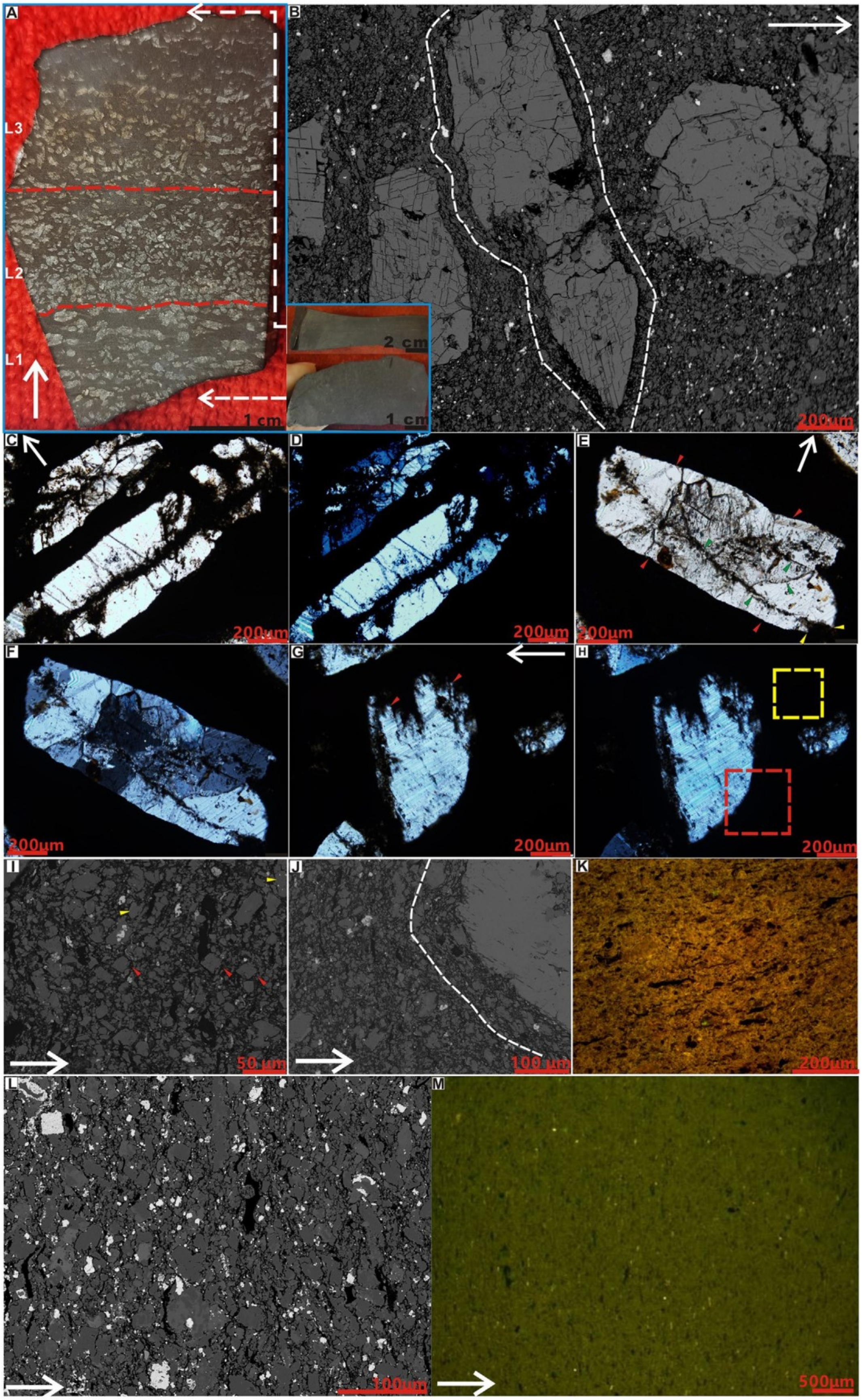
A
B
L3
L2
L1
2 cm
1 cm
1 cm
200μm
C
D
E
200μm
200μm
200μm
F
G
H
200μm
200μm
200μm
I
J
K
50 μm
100 μm
200μm
L
M
100μm
500μm

Table 1

Mineral composition, Rock Eval pyrolysis, and biomarker parameters of TMC in the Lucaogou Formation. The average data of Shale[a] is cited from Liu et al. (2017); Shale[b] is Hackley et al. (2016); Shale[c] is Jiao et al. (2020); M10O and M10U are the overlaying and underlaying TM, respectively; Mineral compositions were detected by XRD; Cal-calcite, Qz-quartz, Plc-plagioclase, Kf-K-feldspar, Dol-dolomite, Py-pyrite; TOC-total organic carbon, S_1-free hydrocarbons, S_2-hydrocarbon generated during Rock Eval pyrolysis, $S_1 + S_2$-generative potential,

HI-hydrogen index, PI-production index, Calculated $R_o = (T_{max}*0.018)-7.16$; $OEP = (C_{15} + 6C_{17} + C_{18})/[4(C_{16} + C_{18})]$, $CPI = 2(C_{23} + C_{25} + C_{27} + C_{29})/[C_{22} + 2(C_{24} + C_{26} + C_{28}) + C_{30}]$, Pr/Ph = Pristane/Phytane, Pr/C_{17} = Pristane/C_{17}n-alkane, Ph/C_{18} = Phytane/C_{18}n-alkane, $C_{27}\%$ = C_{27} steranes/(C_{27} steranes + C_{28} steranes + C_{29} steranes), Homohopanes C_{31}S/ R = Homohopanes C_{31}22S/(22S + SSR), GI = Gammacerane/C_{30}hopane.

Sample	Mineral composition						TOC	S_1	S_2	Tmax	S_1+S_2	HI	PI	Calculated Ro
No.	Cal	Qz	Plc	Kf	Dol	Py	(%)	(mg/g)	(mg/g)	(°C)	(mg/g)	(mg/g)		
M10-D-1	46.7	15.1	24.1	4.3	7.2	2.6	6.07	3.13	39.39	440	42.52	648.93	0.07	0.76
M10-D-2	45.8	13.9	30.6	2.3	7.1	0.3	6.41	3.21	38.06	446	41.27	593.76	0.08	0.87
M10-D-3	52.1	8.1	30.3	2.2	6.9	0.4	7.93	2.98	38.71	438	41.69	488.15	0.07	0.72
M10-D-4	54.8	7.2	29.4	2.8	5.8	0	7.14	3.11	39.12	440	42.23	547.9	0.07	0.76
M10-D-5	34.8	13.8	36.8	6.7	6.6	1.3	6.78	3.23	38.52	442	41.75	568.14	0.08	0.80
Average	46.8	11.6	30.2	3.7	6.7	0.9	6.87	3.13	38.76	441.2	41.89	569.38	0.07	0.78
M10O	0	28.7	45.8	15.4	8.1	2.0	3.43	2.00	14.89	439	16.98	437	0.12	0.74
M10U	0	20.5	54.6	16.6	6.1	2.2	3.44	1.42	26.47	435	27.89	769	0.05	0.67
Shale[a]	n = 101						4.25	1.52	23.31	443.82	24.83	467.13	0.07	0.83
Shale[b]	n = 10						5.58	2.46	36.62	445.8	39.07	648.26	0.07	0.86
Shale[c]	n = 28						4.86	2.77	28.44	–	31.22	–	0.11	–

	OEP	CPI	C_{21}-/C_{22}+	Pr/Ph	Pr/n-C_{17}	Ph/n-C_{18}	$C_{27}\%$	$C_{28}\%$	$C_{29}\%$	C_{27}/C_{29} Steranes	C_{28}/C_{29} Steranes	C_{31} Homohopanes S/R	C_{32} Homohopanes S/R	GI	Gammacerane/ $0.5C_{31}\alpha\beta$ (22R + 22S)
M10	1.29	1.47	0.94	0.51	0.97	2.27	22.03	46.12	31.84	0.69	1.45	0.49	0.34	0.35	5.07
M10O	0.97	1.56	1.03	1.01	1.00	1.46	22.87	31.58	45.55	0.45	0.87	0.56	0.45	0.12	0.95
M10U	1.24	1.75	3.52	1.40	1.46	1.29	22.05	32.80	45.15	0.48	0.88	0.48	0.35	0.37	3.75
Shale[a]	n = 27	–	–	0.91	0.70	0.81	–	–	–	–	0.75	–	–	0.25	–
Shale[b]	n = 5	1.10	–	1.12	0.59	0.65	15.8	39.4	44.8	0.35	0.88	–	–	–	–

inclusions and organic matter in the matrix were documented for comparative study using fluorescence spectrophotometer in Xi'an Shiyou University, China.

Organic geochemical characteristics were documented to interpret the relationship between the calcite grains and hydrocarbon generation. The powders of five laminae in Sample M10-D and in samples M10O and M10U were collected by micro-drilling for pyrolysis and X-ray diffraction (XRD) analysis. Samples M10-D, M10O, and M10U were powdered (<200 mesh) for biomarker analysis. The biomarker sample was extracted by Soxhlet extraction for 72 h to fractionate saturate-aromatic-resinasphaltene. The saturated and aromatic hydrocarbon fractions were analyzed using aTRACE1300-ISQQD300 chromatograph-mass spectrometer. All the above analyses were conducted in the Department of Geology, Northwest University, China.

4. Results

4.1. Petrographic characteristics

Generally, the fine-grained sedimentary rocks in the Lucaogou Formation are composed of mm-scale laminated tuffaceous shale and dolostones (Liu et al., 2012; Jiao et al., 2020; Pan et al., 2020; Zhang et al., 2021). In some cases where laminations are absent, the shale is termed as tuffaceous mudstone. The studied sand-sized calcite grains occur in the tuffaceous mudstone with 2–5 cm thick beds. Their underlying and overlying beds are also tuffaceous mudstones (Fig. 2A). The mudstone overlies a tuff and underlies a tuffaceous shale (Fig. 1E). Those lithofacies are gray to black and serve as shale oil reservoirs in the Lucaogou Formation in the Santanghu Basin (Hackley et al., 2016; Liu et al., 2017). In this paper, we refer the tuffaceous mudstone containing sand-size calcite grains as TMC for short; while the tuffaceous mudstone without calcite grains is TM.

4.1.1. Tuffaceous mudstone containing sand-sized calcite grains

Generally, the mudstone containing sand-sized calcite grains (TMC) is massive and intercalated with tuffaceous mudstones without the calcite grains (TM) with gradational boundaries at the upper part (Fig. 2A). The calcite grains have a constant width of ~500 μm and variable length of 100 μm to 2 mm, and are scattered in the silt to clay-sized non-calcitic matrix (Fig. 2A, B). The grains are dominantly polycrystalline, rarely monocrystalline, and have smooth edges along the long axis, and angular saw-toothed edges along the short axis (Fig. 2C–H). Many microcracks occur in the grains (Fig. 2B–F). The studied core of TMC contains three crude laminae with gradational boundaries and a variable amount of calcite grains of varying size, morphology, and orientation (Fig. 2A). In the lower lamina (L1 in Fig. 1A), the grains are the largest, mainly polycrystalline, ranging mostly from 800 to 1800 μm long, few ~500 μm, crudely bedding-parallel (Fig. 2C, D), and account for 35% of the lamina. In the middle lamina (L2), calcite grains are randomly oriented, and account for ~50% of the limina. The polycrystalline calcite grains account for ~70% of all calcite grains and range from 1000 to 1500 μm in length (Fig. 2E, F), whereas the monocrystalline grains account for

Fig. 2. Photomicrographs of sedimentary structure and texture of sand-sized calcite grains. White arrows show direction of stratigraphic-up. A. A vertical cut of core showing sedimentary structures of the tuffaceous mudstone containing sand-sized calcite grains (TMC) and its underlying and overlying tuffaceous mudstones (TM; white dashed lines). The calcite grains are very coarse to coarse sand-sized, moderately sorted, angular, and discrete in the gray matrix. B. The calcite grains are angular with clear cleavages (straight black lines) and microcracks (irregular black lines). Grains close to the calcite grains in the matrix (marked by white dashed lines) are oriented along the edge of the calcite grains. C. A close-up of L1 in (A) showing elongate calcite grains. PL. D. The same area as (C) showing calcite grains under XL. The grains are polycrystalline calcite. E. A close-up of L2 in (A). The calcite grain is very coarse sand in size, has straight (red arrows) and angular (yellow arrows) edges, and many microcrack (green arrows). PL. F. The same area as (E). The calcite grain is a polycrystalline calcite. XL. G (PL) & H (XL). A single calcite grain in L2 in (A) of a medium sand size, showing angular edges with sharp convex-concave fracture surfaces (red arrows). The yellow and red dashed boxes are the location of (I and J), respectively. I. A close-up of the matrix. Grains in matrix

are mainly randomly distributed except those close to the calcite grain. They are mainly silt to clay sized and angular albite with minor dolomite (red arrows) and subrounded quartz (yellow arrows). Organic matter (black) serves as intergranular pore fillings. BE. J. A close-up of the conformable contact (marked by white dashed line) between a calcite grain and grains in matrix. K. Fluorescent images under incident blue light of the yellow dashed box in (I), showing the characteristics of organic matter in matrix. Yellowish-brown amorphous, laminated alginites are rich in the matrix. L. The underlying tuffaceous mudstone is composed mainly of euhedral feldspars. White grains are pyrite. BE. M. Fluorescent images under blue incident light of the underlying mudstone. PL- plane-polarized light; XL- cross-polarized light; BE- backscatter electron microprobe image. (For interpretation of the references to color in this figure legend, the reader is referred to the web version of this article.)

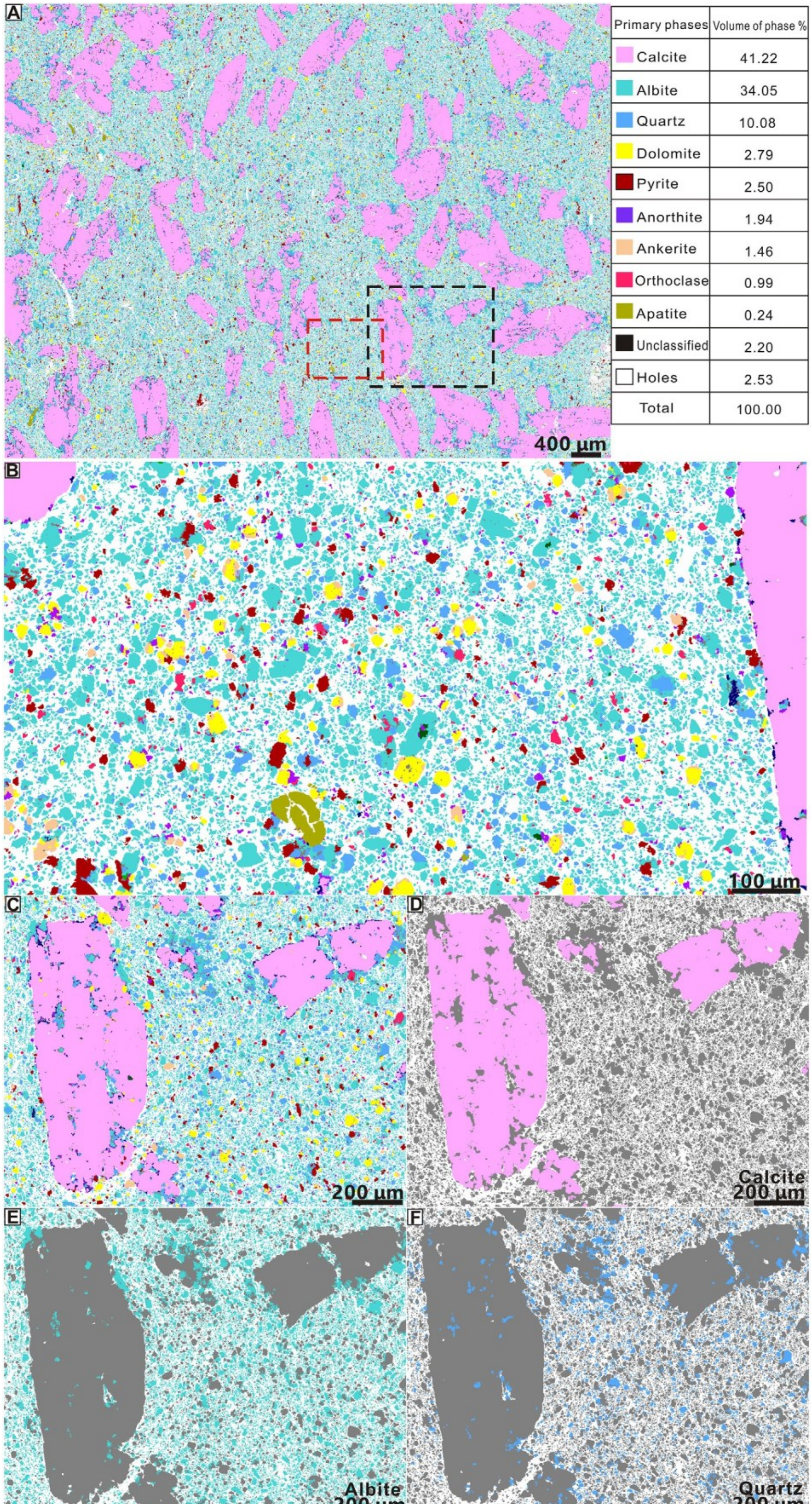

Primary phases	Volume of phase %
Calcite	41.22
Albite	34.05
Quartz	10.08
Dolomite	2.79
Pyrite	2.50
Anorthite	1.94
Ankerite	1.46
Orthoclase	0.99
Apatite	0.24
Unclassified	2.20
Holes	2.53
Total	100.00

Fig. 3. Tescan Integrated Mineral Analyzer (TIMA) image showing mineral composition and texture of TMC. A. An overall image of the studied sample. Different colors represent different minerals. Their names and volumes (%) are shown on the right part. B. Close-up of red dashed box in (A). The white area between minerals is pores which are filled by orgeanic matter. C. Close-up of black dashed box in (A). D. The same area as (C). An artificial-single phase image of calcite grains (purple; other minerals are gray), showing that calcite only occurs as sandsized grains, not present in matrix. E. The same area as (C). A single phase image of albite showing that albite grains mainly occur in matrix and some microcracks in the calcite grains. F.The same as (C), showing the quartz grains. (For interpretation of the references to color in this figure legend, the reader is referred to the web version of this article.)

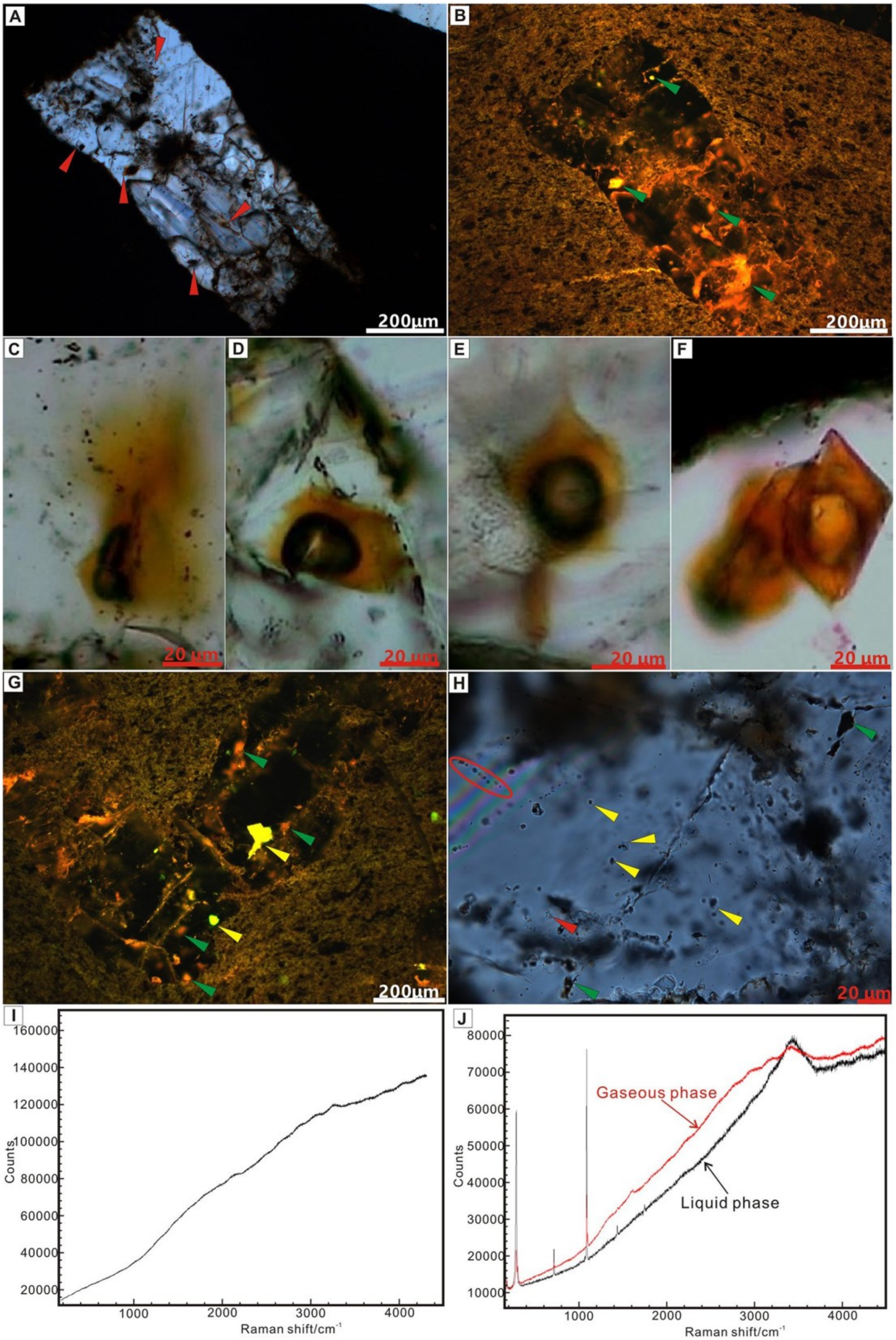

Fig. 4. Photomicrographs of fluid inclusions in sand-sized calcite grains showing their morphology, distribution, and fluorescent color. A. A grain rich in hydrocarbon-rich fluid inclusions (red arrows). PL. B. The same grain as in (A), showing characteristics of organic matter (green arrows) on the grain and in matrix under fluorescence incident blue light. Exposure time is 2 s. C & D. Hydrocarbon-rich inclusions along microcracks or cleavages are elongate along a crack or confined in cleavages. PL. E &F. Isolated hydrocarbon-rich inclusions are mainly rhombic and randomly distributed. PL. G. The rhombic inclusions show yellow color (yellow arrows), whereas the irregular inclusions show orange color (green arrows). Organic matter in microcrack and matrix show similar orange color under

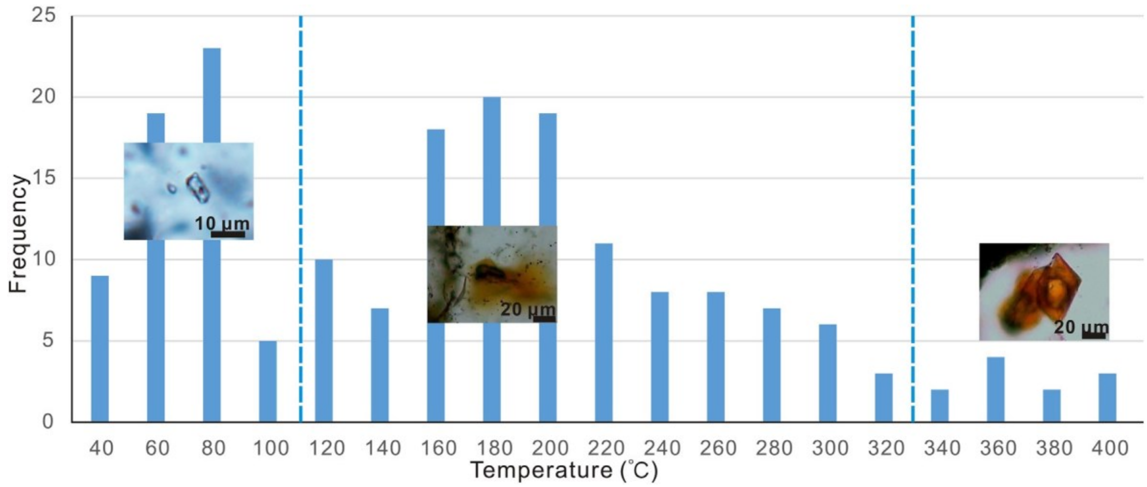

fluorescence incident blue light. H. Hydrocarbon-rich fluid inclusions are abundant and randomly distributed (yellow arrows), and/or along cleavages or micro-cracks in calcite (green arrows). Gas-liquid fluid inclusions are mainly chain-like as secondary inclusions. Red arrow marks a primary inclusion. PL. I. Raman spectrogram of a hydrocarbon-rich fluid inclusion. J. Raman spectrogram of a gas-liquid fluid inclusion. PL- plane-polarized light. (For interpretation of the references to color in this figure legend, the reader is referred to the web version of this article.)

Fig.5. Homogenization temperature distribution of fluid inclusionsin sand-sized calcite grains. Three main ranges of temperature are separatedby blue dashed lines. Images of typical fluid inclusions are shown within the three ranges. (For interpretation of the references to color in this figure legend, the reader is referred to the web version of this article.)

~30% and range from 200 to 500 μm (Fig. 2G, H). Calcite grains in the upper lamina (L3) have similar grain size and orientation to those in the middle lamina, but are less abundant (45%).

The whole-rock mineral composition of the five TMC samples, as obtained by XRD analysis, is calcite (34.8–54.8 wt%, 46.8 wt% on average), plagioclase (24.1–36.8%, 30.2% on average), quartz (7.2–15.1%, 11.6% on average), dolomite (5.8–7.2%, 6.7% on average), K-feldspar (2.2–6.7%, 3.7% on average), and pyrite (0–2.6%, 0.9% on average; Table 1). The composition obtained by TIMA (Fig. 3A, B, C) is similar to that by XRD analysis and is calcite (41.22%), albite (34.05%), and quartz (10.08%) with a minor amount of dolomite, pyrite, anorthite, ankerite, orthoclase, and apatite. Surprisingly, the non-calcite grains are of a silt to clay size and serve as matrix, whereas the calcite grains only occur as framework grains and are sand sized (Fig. 3D–F).

In the matrix, non-calcite grains and organic particles are randomly distributed, except where they are close the calcite grains, they are oriented parallel to the edge of the calcite (Fig. 2B, J). Albite grains are angular and silt to clay-sized, whereas quartz grains are subrounded (Fig. 2I). Organic particles are abundant in the matrix and show bright, amorphous, and laminated fluorescence (Fig. 2K).

4.1.2. Tuffaceous mudstone without sand-sized calcite grains

Tuffaceous mudstones (TM)underlying and overlying the studied TMC have a similar mineral composition and texture (Table 1, Fig. 2L). However, TM is not organic rich as indicated by the dark green fluorescence (Fig. 2M). It is composed dominantly of silt-sized angular plagioclase feldspars (50.2 wt% on average) and K-feldspar (16.0 wt% on average), quartz (24.6 wt% on average), dolomite (7.1 wt% on average), a trace amount of pyrite, and no clay minerals (Fig. 2L). TM is common in the Lucaogou Formation, and is characterized by abundant pyroclastic grains with minor terrigenous quartz and rare clay minerals. It was described in detail by Jiao et al. (2020).

4.2. Characteristics of fluid inclusions

Fluid inclusions in the sand-sized calcite grains are characterized by a hydrocarbon-rich content (Fig. 4A–G). Three types of inclusions were identified on the basis of their distribution, composition, and morphology. The first type contains abundant hydrocarbon and is brown (Fig. 4A, B), and accounts for ~70% of all 100 observed inclusions. The calcite grains containing the inclusions have an irregular or rhombic shape. The irregular inclusions (Fig. 4B–D) are 15–30 μm in size, accounts for ~95% of the hydrocarbon-rich inclusions and have a wide range of homogenization temperature ranging from ~100 to ~320 °C with a peak temperature of ~180 °C (Fig. 5; Table S1). They mainly occur in micro-cracks with anelongated shape (Fig. 4C) or cleavage planes of calcite crystals with a subrhombic shape (Fig. 4D). The inclusions show an orange color under blue fluorescent light (Fig. 4B, G). The rhombic inclusions are not common and have a high homogenization temperature ranging from ~320 °C to ~400 °C (Fig. 5). They are 20–40 μm in size, typically rhombic, and isolated and randomly distributed (Fig. 4E, F). The inclusions show a yellow color under blue fluorescent light (Fig. 4B, G). The second type of inclusions contains mixed gas-liquid, and is 2–5 μm in size, rhombic to elongate in shape, and randomly distributed (Fig. 4H). It accounts for ~20% of all inclusions. The homogenization temperature ranges from 48 to 116.9 °C, with a peak temperature of ~80 °C. The third type of inclusions has a chain-like distribution and is interpreted as secondary inclusions (Fig. 4H) and, thus, is not further studied.

The first and second types of inclusions have a variable chemical composition and degree of maturity of hydrocarbon. First, the Raman spectra of the inclusions show the typical spectrogram of organic matter (Fig. 4I). The exact chemical composition cannot be determined because of the complex signals caused by the high hydrocarbon content. Nevertheless, the gas-liquid inclusions show a dominant content of N_2 and H_2 with a minor amount of CH_4 and liquid water (Fig. 4J; Table 2). Second, the organic particles in the matrix and the irregular-shaped

Table 2
Chemical composition and homogenization temperature of liquid-gas fluid inclusions in sand-sized calcite grains in the studied mudstone. Only data with the analyzed chemical compositions and homogenization temperature are shown. All analyzed data are in supplementary material Table S1.

No.	Size (μm)	Shape	Gaseous phase (%)			Liquid phase (%)	Homogenization temperature(°C)
			CH_4	N_2	H_2	H_2O	
1	2	Rhombus		78	22	100	50
2	3	Rounded		89	11	100	66
3	2	Rhombus	10	72	18	100	75
4	4	Rounded		69	31	100	93
5	5	Elongated		76	24	100	90
6	3	Rhombus		84	16	100	106
7	2	Rounded		82	18	100	82
8	4	Rhombus	7	63	30	100	69
9	5	Rounded		85	15	100	58
10	3	Rhombus		78	22	100	102
11	2	Rounded		74	26	100	90
12	2	Rhombus	6	72	22	100	91
13	5	Rhombus	8	68	24	100	87
14	4	Rhombus	5	75	20	100	116
15	3	Rounded		81	19	100	117

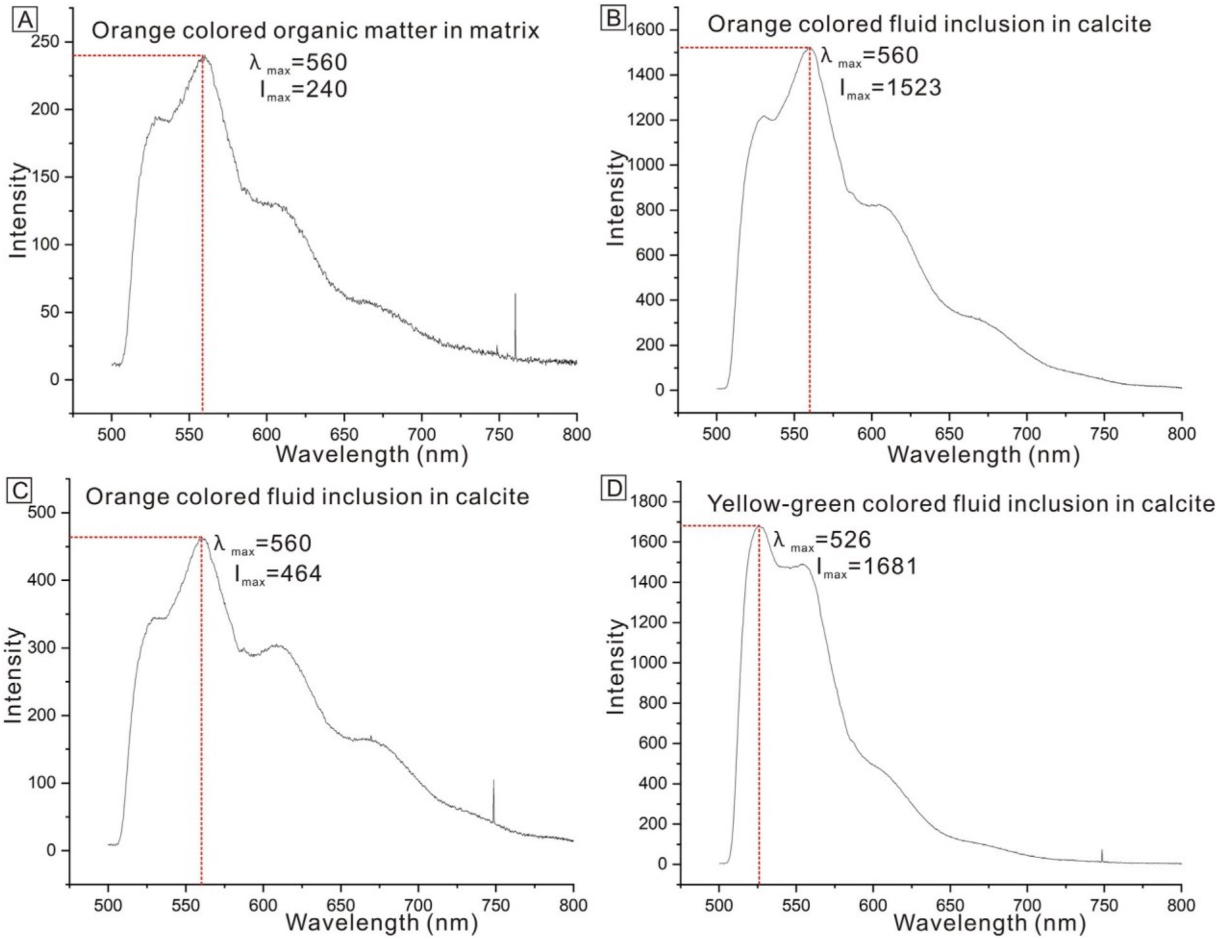

Fig. 6. Microscopic fluorescence spectra of organic matter and fluid inclusions in the calcite-bearing mudstone. I_{max} = maximum spectral intensity; λ_{max} = wavelength corresponding to I_{max}.

hydrocarbon-rich inclusions have the similar orange color under the fluorescence light (Fig. 4B, G) as well as similar microscopic fluorescence spectra with the same wavelength corresponding to a maximum spectral intensity of λ_{max} = 560 (Fig. 6A–C). On the other hand, the rhombic inclusions show a yellow color and their λ_{max} is 526 (Figs. 4B, G, 6D).

Table 3

In-situ $^{87}Sr/^{86}Sr$ ratios, and δ ^{13}C and δ ^{18}O values of sand-sized calcite grains from the Lucaogou Formation. 2SD = 2 times the standard deviation of the population of n (n > 3) repeat measurements of the standards during an analytical session. $(^{87}Sr/^{86}Sr)_0$ is the testing ratio. The concentration of Sr and Rb are conducted by LA-ICP-MS. $(^{87}Sr/^{86}Sr)_i$ is the calculated initial ratio. $(^{87}Sr/^{86}Sr)_i = (^{87}Sr/^{86}Sr)_0 - {}^{87}Rb/^{86}Sr \times (e^{\lambda t}-1)$. $\lambda = 1.42 \times 10^{-11}$, t = 270 Ma, e = 2.718.

Sample No.	$(^{87}Sr/^{86}Sr)_0$	2SD	Sr (ppm)	Rb (ppm)	$(^{87}Sr/^{86}Sr)_i$	Sample No.	δ ^{13}C ‰	δ ^{18}O ‰
M-1	0.705101	0.000099	1216.55	0.095	0.705100	M10-C-1	4.39	−21.70
M-2	0.705236	0.00015	727.72	0.069	0.705235	M10-C-2	4.69	−21.37
M-3	0.705001	0.000151	1196.8	0.083	0.705000	M10-C-3	5.06	−21.18
M-4	0.705051	0.000088	1124.21	0.075	0.705050	M10-C-4	4.24	−21.58
M-5	0.704989	0.000095	849.07	0.07	0.704988	M10-C-5	4.48	−21.63
M-6	0.705122	0.00008	1682.27	0.134	0.705121	Average	4.57	−21.49
M-7	0.705072	0.000098	1580.07	0.079	0.705071			
M-8	0.705287	0.000109	1201.16	0.109	0.705286			
M-9	0.705841	0.000195	1120.18	0.069	0.705840			
M-10	0.705302	0.000093	823.68	0.088	0.705300			
M-11	0.705123	0.000059	1542.17	0.064	0.705123			
M-12	0.705009	0.000079	1610.96	0.069	0.705009			

M-13	0.704932	0.000067	943.64	0.065	0.704932
M-14	0.704997	0.000065	1056.71	0.065	0.704996
M-15	0.705075	0.000063	1260	0.072	0.705075
M-16	0.705124	0.00007	870.77	0.226	0.705121
M-17	0.705145	0.000057	775.16	0.065	0.705144
M-18	0.705130	0.000064	1171.1	0.08	0.705129
M-19	0.705088	0.000061	1711.35	0.103	0.705088
M-20	0.705132	0.000076	1006.26	0.068	0.705131
Average	0.705138		1173.49	0.087	0.705137

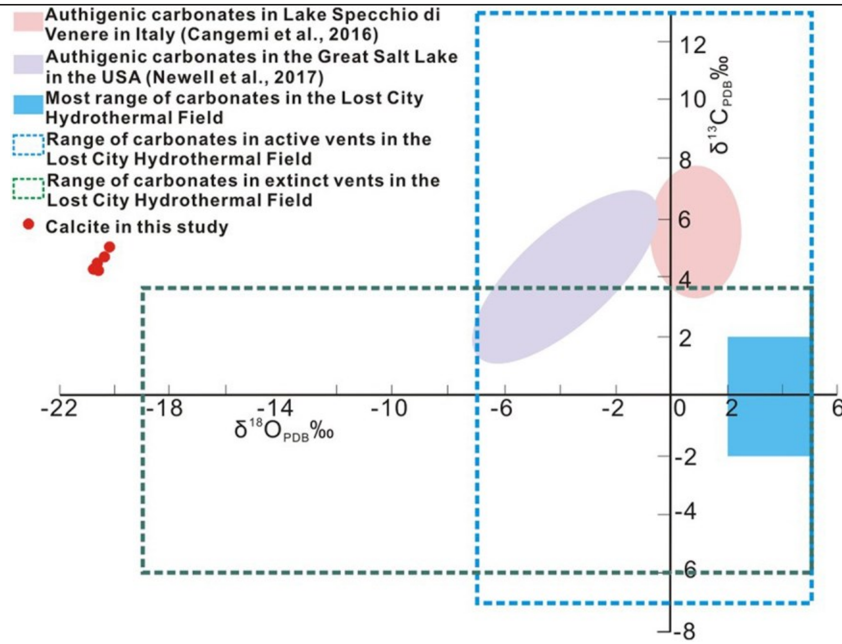

Fig. 7. Carbon and oxygen isotopes of calcite grains.

4.3. In-situ strontium, carbon, and oxygen isotopic and elemental compositions of calcite

In-situ strontium isotope analysis of 20 test points on 20 calcite grains produced an $^{87}Sr/^{86}Sr$ ratio of 0.704932–0.705840, and 0.705137 on average (Table 3). The ratios are lower than those of the Permian global marine carbonate (0.7067 to 0.7085; Burke et al., 1982), and much lower than those of carbonates in the Lost City hydrothermal field (0.7076 to 0.7090; Kelley et al., 2005), but close to the global average of mantle-derived rocks (0.7035; Palmer and Elderfield, 1985). Furthermore, the ratios are much lower than the crustal salic rocks (0.720 ± 0.005; Faure, 1986). The $\delta^{13}C$ values of calcite grains range from 4.24 to 5.06‰, and 4.57‰ on average. In contrast, the $\delta^{18}O$ values are extremly negative, ranging from −21.70 to −21.18‰, and −21.49‰ on average (Fig. 7; Table 3).

Table 4

The major elemental compositions of calcite grains (Table 4) are typical of calcite with Ca (53.22–57.02 wt%, 55.27 wt% on average) and CO_2 (42.15–47.91 wt%, and 44.48 wt% on average). However, some trace metals are relatively abundant, such as Mg (0.14–0.16

wt%, 0.30 wt% on average), Fe (0.23–0.41 wt%, 0.23% on average), and Sr (0.08–0.27 wt%, 0.17% on average). This is very similar to the trace metal enrichment in the calcite in the Lost City hydrothermal field (Kelley et al., 2005). The total REE content (∑REE) of the calcite grains is very low, ranging from 7.38 to 21.93 ppm, and 11.98 ppm on average (Table 5), indicating a low absolute REE concentration in the precipitating fluid. The REE pattern (Fig. 8) shows a clear Eu negative anomaly (δEu ranging from 0.64– 1.03, 0.84 on average) The Ce shows a weakly positive anomaly (δCe ranging from 0.93–1.31, 1.04 on average), The average value of $(La/Lu)_N$ is 0.63, similar to that of carbonates and hydroxide complexes under neutral to mildly basic conditions (Bua, 1991).

The TOC content of the TMC ranges from 6.07 to 7.93 wt%, and 6.87% on average. It is higher than that of the surrounding TM (M10U and M10O; 3.44 wt% and 3.43 wt%) and other common shales in the Lucaogou Formation (Table 1) in the Santanghu Basin, as reported by Hackley et al. (5.58 wt%; 2016), Liu et al. (4.25 wt%; 2017), and Jiao et al. (4.86 wt%; 2020). In addition, the pyrolysis yield (S2) ranges from 38.06 to 39.39. Thus, the TMC has a higher potential as a hydrocarbon source rock than the other shales. Four of the analyzed TMC samples fall in the field of Type I kerogen and one sample in Type II kerogen field in the HI-T_{max} diagram (Fig. 9; Langford and BlancValleron, 1990). The calculated R_o values (Jarvie et al., 2001) range from 0.72–0.87%.

Biomarkers in the TMC are distinctively different from those in TM samples M10U, M10O (Table 1) and other common shales in Lucaogou Formation (e.g., Hackley et al., 2016; Liu et al., 2017). The Pr/Ph ratio is

Major elements of sand-sized calcite grains from the Lucaogou Formation. FeO^T- refers to amount of both ferric and ferrous iron.

Sample No.	CaO	CO_2	MgO	FeO^T	SrO	BaO	Na_2O	MnO	Al_2O_3	K_2O	SiO_2	Total
M-1	55.29	43.47	0.30	0.17	0.15	0.15	0.16	0.07	0.00	0.00	0.00	99.76
M-2	54.54	45.65	0.32	0.41	0.27	0.18	0.07	0.04	0.10	0.01	0.00	101.59
M-3	56.47	42.33	0.25	0.27	0.18	0.22	0.05	0.01	0.01	0.00	0.00	99.79
M-4	56.60	44.16	0.19	0.19	0.23	0.10	0.08	0.12	0.00	0.00	0.00	101.67
M-5	57.02	43.16	0.61	0.25	0.12	0.04	0.01	0.04	0.01	0.00	0.00	101.25
M-6	56.38	44.58	0.14	0.14	0.13	0.01	0.05	0.03	0.00	0.00	0.00	101.45
M-7	54.87	47.91	0.15	0.00	0.12	0.07	0.14	0.00	0.03	0.00	0.00	103.29
M-8	56.28	44.98	0.30	0.26	0.08	0.01	0.00	0.04	0.04	0.01	0.00	101.99
M-9	56.60	43.96	0.39	0.34	0.19	0.05	0.03	0.00	0.04	0.00	0.00	101.60
M-10	55.00	46.06	0.35	0.38	0.22	0.16	0.09	0.06	0.02	0.02	0.00	102.37
M-11	54.38	43.54	0.38	0.21	0.16	0.11	0.14	0.00	0.02	0.01	0.00	98.95
M-12	53.22	44.80	0.26	0.21	0.17	0.13	0.03	0.12	0.00	0.00	0.00	98.94
M-13	53.54	44.69	0.45	0.26	0.18	0.23	0.08	0.02	0.04	0.00	0.00	99.49
M-14	55.46	42.15	0.40	0.27	0.16	0.12	0.04	0.00	0.00	0.00	0.00	98.60
M-15	55.81	42.68	0.15	0.13	0.18	0.15	0.08	0.00	0.01	0.00	0.00	99.19
M-16	56.21	42.77	0.19	0.09	0.17	0.14	0.05	0.02	0.03	0.01	0.00	99.68
M-17	54.16	45.30	0.31	0.28	0.17	0.11	0.08	0.03	0.01	0.02	0.00	100.47
M-18	54.02	46.80	0.22	0.31	0.22	0.14	0.05	0.00	0.01	0.02	0.00	101.79
M-19	54.48	44.81	0.34	0.21	0.16	0.12	0.05	0.01	0.02	0.01	0.00	100.21
M-20	55.01	45.83	0.36	0.27	0.19	0.13	0.07	0.02	0.00	0.01	0.00	101.89
Average	55.27	44.48	0.30	0.23	0.17	0.12	0.07	0.03	0.02	0.01	0.00	100.70

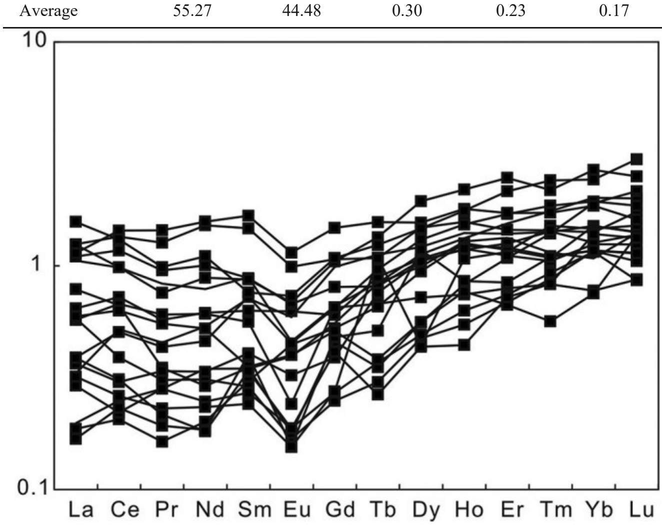

Fig. 8. REE pattern of calcite grains normalized to primitive mantle (Sun and McDonough, 1989).

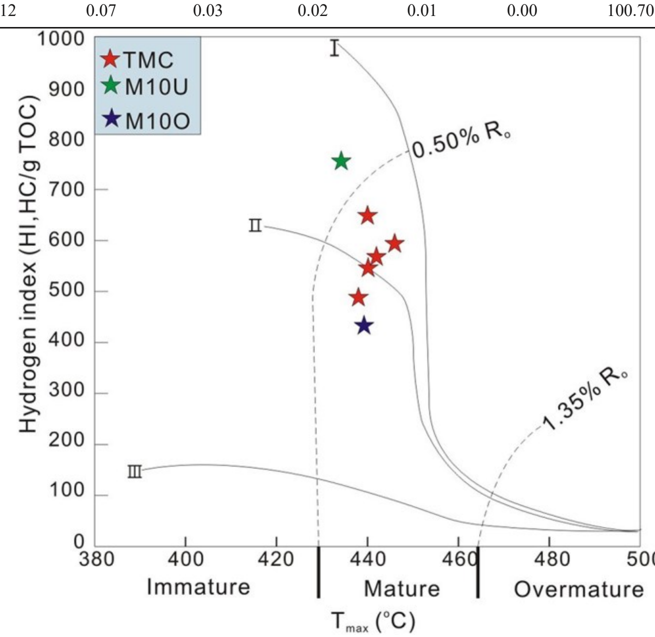

4.4. Characteristics of organic matter

Fig. 9. Plot of HI vs. T_{max} outlining the kerogen types of organic matter in TMC and underlying (M10U) and overlying (M10O) TM (Langford and Blanc-Valleron, 1990).

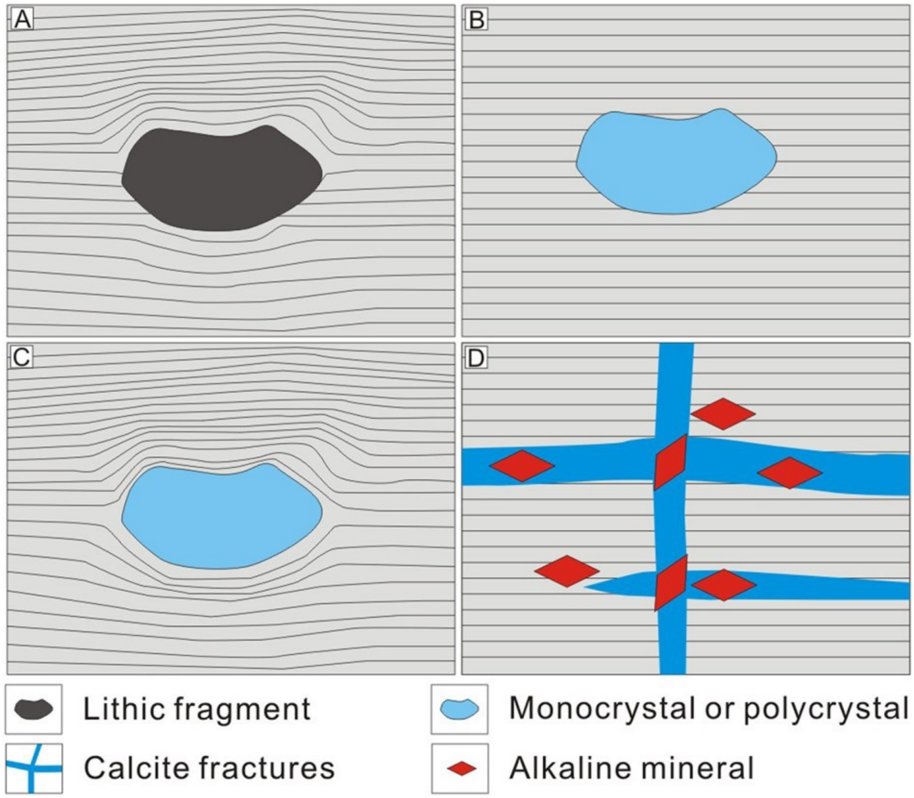

Fig. 12. Sketch showing coarse grains in fine-grained sedimentary rocks. A. An allogenetic-detrital grains in shale. The lower boundary is as subvertical cut contact due to gravity during grain settlement, whereas the upper boundary is conformable and modified by compaction. B. A cave-filling mono- or poly-crystalline nodule after lithification. The nodule has a disconcordant contact with adjacent laminae. C. A nodule formed at the syn-depositional to penecontemporaneous stage. The upper and lower boundaries are conformable. D. Precipitation of alkaline minerals in micro fractures.

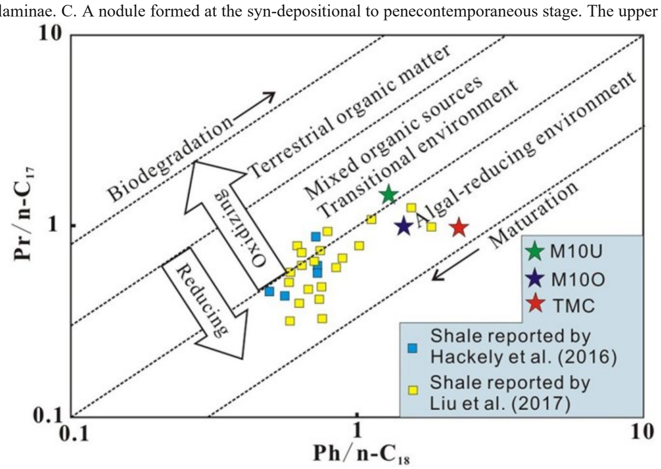

Fig. 10. Cross-correlation of Pr/nC_{17} vs Ph/nC_{18} ratios of the TMC, and its underlying (M10U) and overlying (M10O) TM, and common shale (Hackley et al., 2016; Liu et al., 2017). Classification from Connan and Cassou (1980).

0.51, much smaller than that of TM M10U (1.40), M10O (1.01), and shales reported by Liu et al. (0.66–1.25, 0.91 on average, n = 33; Liu et al., 2017) and Hackley et al. (0.85–1.41, 1.12 on average, n = 5; Hackley et al., 2016). The value of Pr/nC_{17} vs Ph/nC_{18} (Fig. 10) falls in the range of algal/microbial-source of organic matter deposited in a reducing environment, which is different from the mixed terrestrial to algal source of organic matter deposited in reducing environment, as interpreted from the adjacent TM (M10U and M10O). Furthermore, the TMC has a higher degree of maturation than that of the other shales reported by Hackley et al. (2016) and Liu et al. (2017). The gammacerane index (GI) is 0.35; and the gammacerane/$0.5C_{31}\alpha\beta(22R + 22S)$ ratio is 5.07. Finally, the relative proportion of C_{28} steranes is 46.12%, followed by C_{29} 31.84% and C_{27} 22.03%. They display a different pattern (Fig. 11)

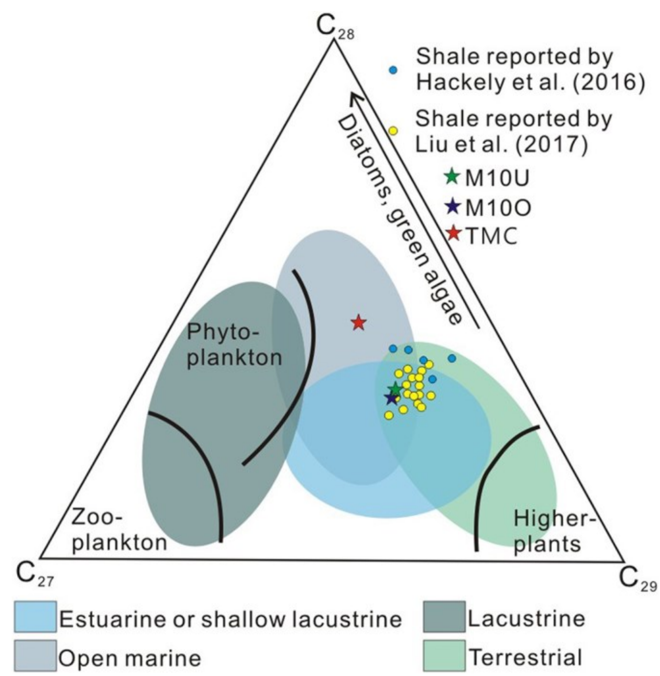

Fig. 11. Normal sterane distribution of the TMC, and the underlying (M10U) and overlying (M10O) TM, and common shales (Hackley et al., 2016; Liu et al., 2017) in Lucaogou Formation. Classification from Liu et al. (2017); interpreted paleoenvironment and source from Huang and Meinschein (1979), Mackenzie et al. (1982), Volkman (1986), Riboulleau et al. (2007), and Farhaduzzaman et al. (2012).

than those of mixed higher plants and algae in the TM (M10U and M10O), and the common shales (e.g., Hackley et al., 2016; Liu et al., 2017).

5. Discussion

5.1. Source of sand-sized calcite grains

The texture of the sand-sized calcite grains and silt-clay-sized grains in matrix in the calcite-bearing tuffaceous mudstones (TMC) indicates that the mudstone was deposited by a high-density debris flow. However, there are two alternative interpretations for the source of the calcite grains, as discussed below.

Sand-sized grains in lacustrine shales are common and generally interpreted as detrital sediments or diagenetic products (Fig. 12; Stow, 2005; Łapcik et al., 2021). The detrital grains may be produced by subaerial volcanic explosion (e.g., White, 2000; de Silva et al., 2013) or glacial melting (e.g., Yang et al., 2007, 2010; Kirkbride and Winkler, 2012; Xu and Yi, 2014; Westoby et al., 2014). They drop into the fine-grained sediments and show sub-vertical cut at the base of the dropstone and comfortable upper surface (Fig. 12A; e.g., Yang et al., 2010). The diagenetic products are precipitates in silica or carbonate oversaturated solutions during the penecontemporaneous stage to form nodules, or vein and cave-fillings in lithified sediments (e.g., Jiao et al., 2018b, 2020; Hackley et al., 2016). These mineral grains can also be secreted by organisms (Siever, 1962; Williams and Crerar, 1985; Jiao et al., 2018b) or generated by volcanic or hydrothermal activities (Adachi et al., 1986; Fischer and Knoll, 2009). Except the cave and vein-filling structures which have uncomfortable contacts (Fig. 12B), the nodules formed during the penecontemporaneous stage generally show comfortable contact with adjacent laminae (Fig. 12C; e.g., Jiao et al., 2020). Hence, the calcite grains may have a similar source with the nodules due to the comfortable contacts with grains in matrix (Fig. 2B, J).

In addition, ancient shales and modern sediments formed in a volcanic and hydrothermal-related alkaline lake contain many mineral assemblages with relatively large grains (e.g., the alkaline lake of the Eocene Green River Formation in U.S.A. and Permian Fengcheng Formation in China; Cao et al., 2020; Guo et al., 2021). Almost all of the grains experienced a significant diagenetic alteration related to salinization and evaporation, which also formed halite, gypsum, and some highly alkaline minerals, such as trona and shortite (Cao et al., 2020). They are euhedral and occur in calcite fractures or intergranular pores associated with some evaporitic sedimentary structures (Fig. 12D; e.g., shrinkage cracks and subaerially-exposed and transported sediments with ripple marks; Garcia-Fresca et al., 2018; Guo et al., 2021). The characteristics of the calcite grains and the grains in matrix (Fig. 2B, J) and the lack of evaporitic features indicate that the calcite grains are not of an evaporitic origin.

Eliminating the possible common origins discussed above, we interpret that the TMC was deposited in a subaqueous lacustrine environment by a high-density debris flow containing feldspar-dominated volcaniclastics and fragmented calcite crystals and a minor amount of terrigenous quartz. First, the non-calcite grains are mainly randomly distributed but oriented parallel to the edge of the calcite in matrix (Fig. 2B, J). This geometry suggests that the calcite grains were deposited together with the other grains. Second, as the dominant noncalcite grain, albite grains are angular and show no or minimal abrasion; while quartz grains are subrounded (Fig. 2I), suggesting that the quartz grains had experienced significant abrasion, probably during current transport. The lack of clay minerals suggest a minimal influx of detrital clay at the depositional site. Hence, the mudstone is composed mainly of pyroclastic deposits with a small amount of terrigenous sediments. Third, the sharp bed contacts without significant erosion, matrixsupported texture without clear lamination (Fig. 2A, B), random grain orientation (Fig. 2A, I), and lack of grain abrasion (Fig. 2B–J) all point to a subaqueous density debris flow deposit (Mulder and Alexander, 2001). The similar width (~500 μm) and various length, angular edges along the short axis, and abundant inner micro-cracks of the calcite grains (Fig. 2B–H) suggest extensive fragmentation of calcite ripped from a calcitic parent rock. Perhaps, that parent rock is laminae or veins composed of precipitated calcite crystals with an individual thickness of 0.5 mm. On the other hand, the significantly different mineral composition of the matrix suggests that the matrix and calcite grains were not derived from the same source rock and were mixed together during sediment transport and/or deposition.

5.2. Environment and conditions of formation of sand-sized calcite grains

The carbon isotopic values are similar to those of autogenetic carbonates in alkaline lakes influenced by a variety of volcanichydrothermal and biological activities (Fig. 7; Cangemi et al., 2016; Newell et al., 2017) and to those of the carbonates in the Lost City Hydrothermal Field (Kelley et al., 2005). The positive excursion of $\delta^{13}C$ of lacustrine carbonates is common in a volcanic-hydrothermal influenced alkaline lake, where evaporation (Talbot and Kelts, 1990; Liu et al., 2001; Cangemi et al., 2016; Newell et al., 2017) and/or microbial activities (Mazzullo, 2000; Wacey et al., 2007) can produce carbonate minerals enriched with ^{13}C.

In the meanwhile, the oxygen isotopic values are very different from the carbonates in alkaline lakes and those, mainly microcrystalline aragonite and calcite, in active vents in the Lost City hydrothermal field.

Only the carbonates in extinct vents in the hydrothermal field, where carbonates (mainly mega-cryastlline calcite) were altered and recrystallized by hydrothermal fluid over a long time period, have negative values down to −19‰ (Kelley et al., 2005). Commonly, influx of fresh water and/or hydrothermal fluid during carbonate precipitation can cause enrichment of ^{16}O (Boni et al., 2000). For example, the $\delta^{18}O$ value of hydrothermally altered carbonate reservoirs can decrease to −18‰ (Davies and Smith, 2006; Lonnee and Machel, 2006; Smith, 2006). In the modern carbonate-precipitating hydrothermal fields, mineral assemblages are anhedral microcrystalline aragonite and brucite at active vents, and gradually change to well crystallized calcite with a negative $\delta^{18}O$ value at the extinct vent (Kelley et al., 2005). This trend indicates that continuous hydrothermal activities alter the mineralalogy and isotopic composition, which is coincident with the studied calcite grains with well crystallized form and strongly negative $\delta^{18}O$ values. Furthermore, evaporatic processes preferentially vaporize ^{16}O into atmosphere to enrich ^{18}O in carbonate precipitates (Talbot and Kelts, 1990; Liu et al., 2001). However, the lack of evidence of evaporation and rarity of terrigenous sediments indicate minimal fresh water influx. Hence, the calcite may have been formed by hydrothermal fluids. First, the homogenization temperature (79.1 °C on average) of gasliquid inclusions (Fig. 4H) supports a hydrothermal influence. Second, the Sr isotope ratios of the calcite grains suggest that the fluid from which the calcite was precipitated has a mixed origin of mainly mantle-derived fluid and a small amount of lake water. The temperature range and chemical composition are similar to those of the carbonates formed in the low-temperature Lost City Hydrothermal Field near the Mid-Atlantic Ridge (Kelley et al., 2001). The modern hydrothermal

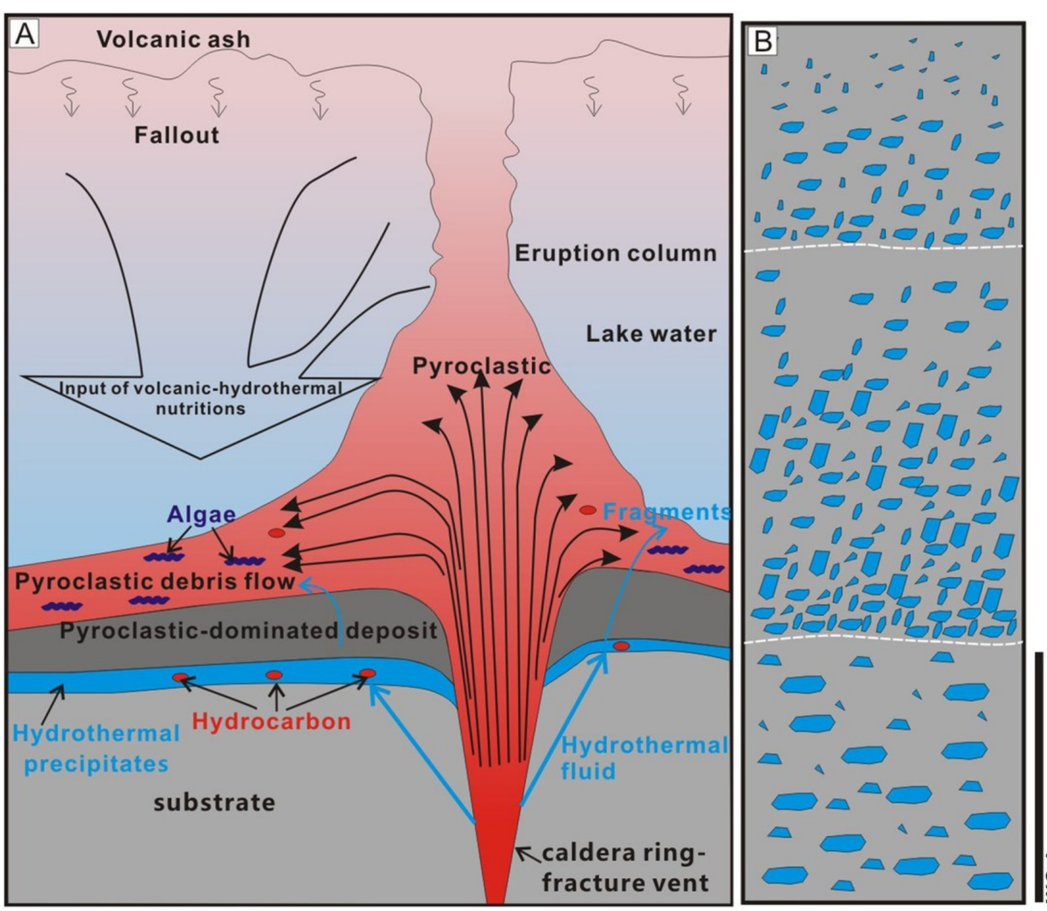

Fig. 13. A. Depositional model for the TMC in the Santanghu volcanic lake (modified after Kokelaar and Busby, 1992; no scale intended). The lake was influenced by subaqueous volcanichydrothermal activities. Hydrocarbons generated from microbially-originated organic matter and derived from a deep source accumulated together in the mudstone. B. Simplified sketch showing the sedimentary structures and textures of the TMC. The blue grains are the sand-sized calcite grains, and the gray background represents the matrix. (For interpretation of the references to color in this figure legend, the reader is referred to the web version of this article.)

fields commonly have two distinctive areas on the basis of temperature, chemical composition, and distance from the volcanic center (Kelley et al., 2001, 2005; Genna et al., 2014). The area close to the center is characterized by a high temperature ranging from 273 to 370 °C and volcanigenic massive sulfide (VMS) deposits (Kelley et al., 2001) with a positive Eu anomaly (Genna et al., 2014). On the other hand, the distal area has a relatively low temperature (e.g., 40 to 75 °C in the Lost City hydrothermal fleid; Kelley et al., 2001) and contains carbonate deposits with volcanic glass and plagioclase with a negative Eu anomaly (Genna et al., 2014). Bua (1991) found that a high temperature (up to 600 °C) regime can fractionate other REE to Eu, resulting in a positive Eu anomaly. In relatively low temperature conditions, hydrothermal or metamorphic fluid-rock interaction, for example, will cause a negative Eu anomaly and an extremely low REE content. Hence, the negative Eu anomaly and low REE content (Fig. 8) of the calcite grains support a relatively low temperature hydrothermal condition.

Finally, the characteristics of some trace elements indicate a saline and reducing environment during the formation of calcite grains. A Y/ Ho ratio > 28 generally indicates marine water or saline lake water (Cao et al., 2020). The range of Y/Ho ratio of the calcite grains is 27.48 to 57.29, and 32.07 on average (Table 5), indicating that they were formed in a high-salinity water. Besides, elements of U, Th, V, Ni, and Cr are widely applied to reflect the redox state. For example, U/Th >1.25, V/(V + Ni) >0.45, and V/Cr >2 all indicate anoxic environments (Cao et al., 2020). Those ratios of the calcite grains are 1.01, 0.99, and 4.99 on average (Table 5), respectively, suggesting an anoxic condition, although the U/Th ratio indicates a dysoxic condition.

Above all, the in-situ geochemical data of the calcite grains indicate that the calcite grains were formed in a dominantly mantlediverved fluid mixed with a hydrothermally influenced saline and reducing lake water.

5.3. Depositional environment for tuffaceous mudstone containing sand-sized calcite grains

The biomarker parameters of the TMC indicate an anoxic and saline palaeoenvironment, as interpreted from other evidence above. Generally, a Pr/Ph ratio <1 and >1 indicate reducing and oxidizing environmental conditions, respectively (Didyk et al., 1978; Hao et al., 2011). Comparing with the ratios of the underlying and overlying TM with Pr/Ph ratios of 1.24 and 0.97, respectively, the TMC with a Pr/Ph ratio of 0.51 was likely deposited in a highly anoxic environment. In addition, a value of gammacerane index >0.1 suggests an anoxic, saline, and waterstratified sedimentary environment (Liu et al., 2020). Moreover, as an indicator of salinity, the ranges of ratio of gammacerane/0.5$C_{31}\alpha\beta$ (22R + 22S) smaller than 0.3, between 0.3 and 0.5, and larger than 0.5 are interpreted as fresh, brackish, and saltwater, respectively (Li et al., 2017). The value of the gammacerane/0.5$C_{31}\alpha\beta$ (22R + 22S) ratio of our samples is up to 5.07, indicating that the TMC was deposited in a highly saline water. Finally, the relative proportion of C_{27}, C_{28}, and C_{29} (Fig. 11) lies in the paleoenvironment field of open marine, instead of the mixed fields of terrestrial, shallow lacustrine, and open marine (Farhaduzzaman et al., 2012) for the TM and the common shale in Lucaogou Formation (Hackley et al., 2016; Liu et al., 2017). Considering the values of gammacerane index and gammacerane/0.5$C_{31}\alpha\beta$(22R + 22S) ratio and the lacustrine setting of the TMC, the proportion of C_{27}, C_{28}, and C_{29} is interpreted to indicate a lake water that is much more saline than that of the other shales in the Lucaogou Formation.

Table 5

Some trace and rare-earth elemental compositions (ppm) of sand-sized calcite grains in the Lucaogou Formation. Normalized to primitive mantle (Sun and McDonough, 1989).

Sample No.	M-1	M-2	M-3	M-4	M-5	M-6	M-7	M-8	M-9	M-10	M-11	M-12	M-13	M-14	M-15	M-16	M-17	M-18	M-19	M-20	Average
V	48.30	41.57	49.30	52.81	47.15	39.44	60.49	53.39	56.86	34.58	46.02	29.76	55.87	68.29	45.49	55.33	52.80	49.79	41.73	56.26	49.26
Cr	8.31	7.52	11.79	11.00	8.00	6.88	10.04	10.70	8.79	6.56	9.05	6.50	17.83	18.28	11.58	12.14	10.86	10.95	7.62	10.83	10.26
Ni	0.30	0.17	0.26	0.32	0.11	0.26	0.20	0.10	0.58	0.15	0.19	0.09	0.30	0.14	0.11	0.24	0.25	0.25	0.33	1.56	0.30
Th	0.01	0.01	0.01	0.01	0.01	0.01	0.01	0.01	0.07	0.01	0.02	0.01	0.01	0.01	0.01	0.01	0.01	0.01	0.01	0.05	0.02
U	0.01	0.01	0.01	0.01	0.01	0.01	0.01	0.01	0.04	0.01	0.02	0.01	0.01	0.01	0.01	0.01	0.01	0.01	0.01	0.02	0.01
La	0.46	0.14	0.41	0.78	0.13	0.41	0.21	0.56	0.23	0.23	0.88	0.26	0.12	0.75	0.42	0.88	0.28	0.81	0.27	1.11	0.47
Ce	1.33	0.46	1.24	2.14	0.38	0.71	0.40	1.22	0.48	0.95	2.47	0.55	0.42	1.80	1.15	1.80	0.93	2.63	0.57	2.40	1.20
Pr	0.16	0.08	0.17	0.27	0.05	0.09	0.08	0.10	0.06	0.13	0.35	0.09	0.05	0.23	0.15	0.21	0.12	0.40	0.06	0.27	0.16
Nd	0.84	0.47	0.83	1.37	0.27	0.42	0.34	0.40	0.32	0.73	2.07	0.46	0.25	1.07	0.72	1.21	0.63	2.15	0.25	1.51	0.82
Sm	0.28	0.15	0.25	0.39	0.14	0.13	0.12	0.16	0.11	0.32	0.65	0.18	0.18	0.39	0.16	0.39	0.32	0.74	0.15	0.34	0.28
Eu	0.11	0.07	0.04	0.11	0.07	0.03	0.03	0.03	0.03	0.10	0.17	0.05	0.03	0.08	0.07	0.12	0.08	0.19	0.03	0.12	0.08
Gd	0.36	0.33	0.39	0.48	0.31	0.15	0.16	0.27	0.16	0.59	0.64	0.23	0.29	0.39	0.30	0.62	0.39	0.88	0.25	0.64	0.39
Tb	0.10	0.09	0.07	0.09	0.07	0.03	0.04	0.04	0.12	0.12	0.12	0.08	0.06	0.09	0.04	0.14	0.10	0.17	0.03	0.13	0.09
Dy	0.79	0.83	0.53	0.78	0.70	0.35	0.36	0.41	0.33	0.89	1.09	0.77	0.87	0.73	0.41	1.43	0.96	1.15	0.32	1.08	0.74
Ho	0.20	0.22	0.12	0.19	0.21	0.09	0.10	0.13	0.18	0.23	0.26	0.19	0.14	0.21	0.12	0.36	0.25	0.29	0.07	0.29	0.19
Er	0.58	0.74	0.38	0.60	0.56	0.33	0.36	0.52	0.55	0.67	0.69	0.53	0.40	0.64	0.32	1.18	0.81	0.82	0.35	1.03	0.60
Tm	0.08	0.13	0.06	0.11	0.08	0.06	0.07	0.10	0.11	0.10	0.11	0.08	0.08	0.08	0.04	0.16	0.14	0.13	0.06	0.18	0.10
Yb	0.56	0.97	0.37	0.61	0.72	0.56	0.56	0.91	0.70	0.72	0.68	0.60	0.56	0.52	0.36	1.29	0.93	0.89	0.67	1.17	0.72
Lu	0.08	0.15	0.06	0.10	0.10	0.08	0.06	0.16	0.11	0.10	0.13	0.09	0.08	0.10	0.10	0.18	0.14	0.12	0.10	0.22	0.11
Y	5.52	6.45	3.91	5.70	5.33	2.74	2.88	3.77	4.97	6.41	7.22	5.00	3.09	5.60	5.79	10.29	7.19	8.27	2.35	9.36	5.59
∑REE	11.44	11.27	8.83	13.71	9.12	6.17	5.76	8.77	8.45	12.30	17.52	9.17	6.62	12.69	10.16	20.25	13.26	19.63	5.51	19.85	11.52
LREE/HREE	1.15	0.40	1.48	1.71	0.38	1.09	0.69	0.96	0.54	0.72	1.78	0.62	0.42	1.56	1.56	0.86	0.63	1.56	0.73	1.22	1.00
δEu	1.02	0.87	0.40	0.80	1.07	0.63	0.69	0.44	0.60	0.69	0.78	0.82	0.35	0.59	0.92	0.72	0.65	0.73	0.50	0.80	0.70
δCe	1.19	1.04	1.15	1.14	1.18	0.87	0.77	1.17	0.95	1.33	1.07	0.86	1.28	1.04	1.10	0.99	1.23	1.11	1.03	1.03	1.08
U/Th	0.91	1.00	0.51	0.81	1.39	1.86	1.00	1.39	0.54	0.81	0.76	1.00	1.00	1.00	1.33	0.69	0.98	0.85	1.89	0.54	1.01
V/(V + Ni)	0.99	1.00	0.99	0.99	1.00	0.99	1.00	1.00	0.99	1.00	1.00	1.00	0.99	1.00	1.00	1.00	1.00	0.99	0.99	0.97	0.99
V/Cr	5.81	5.53	4.18	4.80	5.89	5.73	6.02	4.99	6.47	5.27	5.09	4.58	3.13	3.74	3.93	4.56	4.86	4.55	5.48	5.19	4.99
Y/Ho	27.60	29.86	32.29	29.69	26.00	30.80	28.10	28.11	28.37	28.11	28.20	25.77	22.22	26.79	46.39	28.82	28.88	28.32	32.57	32.61	29.48
$(La/Lu)_N$	0.57	0.10	0.66	0.80	0.13	0.56	0.34	0.36	0.21	0.23	0.72	0.29	0.15	0.75	0.43	0.49	0.21	0.71	0.29	0.53	0.43

5.4. Hydrocarbon generation in tuffaceous mudstone containing sand-sized calcite grains

The total organic carbon (TOC) content of the TMC is greater than that of common shale and the underlying and overlying TM in the Lucaogou Formation (Table 1). The matrix contains abundant organic particles (Figs. 2K, 4B, G). The relative proportion of C_{27}, C_{28}, and C_{29} (Fig. 11) suggests a mixed organic source dominated by algae (Huang and Meinschein, 1979; Mackenzie et al., 1982; Volkman, 1986). Algal blooms induced by volcanic-hydrothermal activities (Xie et al., 2010) may be the main source of the alginite.

However, hydrocarbon generation commonly depends on temperature threshold which may be controlled by burial depth. In this study, it is hard to speculate the depth of the hydrocarbon generation. However, some inorganic evidence may suggest a weak diagenesis during burial in the Lucaogou Formation. Only some diagenetic features during syndepositional and early burial stages can be observed. First, the welldeveloped dolomite in the Lucaogou Formation has experienced weak diagenesis. The evidence supporting this interpretation includes rare recrystallization and low cation ordering of dolomite, well-preserved dolostone laminae and abundant biological remains. Typical dolomite with a zonal texture under CL formed during burial stage are not well developed (Liu et al., 2012). Second, clay minerals are rare and mainly smectite that is commonly altered from volcanic ash. The alteration should have occurred rather easily during burial (Zhu et al., 2017; Gill, 2010). Third, many shard-like volcanic vitric grains are still well preserved in this formation. Some of them were altered into analcite (Jiao et al., 2020). This alteration also could have occurred easily during early burial (Gill, 2010). Hence, the limited occurrence of these alterations indicates very weak diagenesis occurred during deep burial; and the main hydrocarbon generation occurred during early stage. If hydrocarbon generation occurred at a great burial depth, common and strong diagenetic alterations of minerals should also be present. The two types of hydrocarbon inclusions in the calcite grains (Fig. 4) indicate the generation of hydrocarbons from the mudstone during early burial and suggest some other possible hydrocarbon sources during the formation of calcite grains. The rhombic hydrocarbon-rich and gas-liquid inclusions are primary inclusions as indicated by their euhedral shape and isolated distribution (Fig. 4). Generally, a low λ_{max} value and yellow color of hydrocarbon inclusions indicate a more mature oil in the inclusions than those with a large λ_{max} and orange color (Ryder, 2005; Liu and Eadington, 2005; Si et al., 2020). Hence, the hydrocarbons in the rhombic inclusions are likely more mature. The chemical composition and homogenization temperature of the rhombic inclusions indicate that the hydrocarbon was charged at a relatively early episode during the formation of the calcite grains and may have been influenced by a combination of hydrothermal activities and early burial diagenesis, resulting in a high hydrocarbon maturity. The irregular-shaped inclusions, on the other hand, probably formed after the deposition of the calcite grains. The hydrocarbon was charged during the healing of micro-cracks and cleavages of the calcite in a late burial episode. This interpretation is supported by the distribution, irregular shape, and similar fluorescence color of the inclusions (Fig. 4B, G) and microscopic fluorescence spectra of organic matters in the matrix (Fig. 6).

The occurrence and characteristics of the rhombic hydrocarbon-rich inclusions in the TMC are similar to the “hydrothermal petroleum” in many rift basins and ocean troughs worldwide as reported by Simoneit (1984); Simoneit et al. (2000). A mass of nutrients different from that in normal aqueous environments promoted the bloom of hydrocarbon-generating organisms (Xie et al., 2010; Wright, 2012; Ciotoli et al., 2013; Lee et al., 2018; Procesi et al., 2019), and provided inorganic materials (e.g., CO_2 and CH_4) to form inorganic gas accumulations (Dai et al., 2005). Some hydrocarbon may have migrated from the underlying strata by hydrothermal fluid and/or was generated directly by inorganic CO and H_2 from volcanic-hydrothermal activities through the Fischer-Tropsch process (Simoneit, 1984; Hyatt, 1984; Liu et al., 2019). Methane may have been directly originated from mantle, as indicated by the composition of fluid inclusions. These hydrocarbons provided extra supply for hydrocarbon accumulation. Unfortunately, further evidence is lacking to substantiate the interpretation, such as carbon isotope of the hydrocarbon in the euhedral hydrocarbon-rich inclusions (Fig. 4E, F), which was not obtained due to the limited samples. Nevertheless, the relatively higher maturity and early charging of the hydrocarbons argue for a possible inorganic origin. Our recent research shows that the mudstones without abundant carbonate minerals (TM) have a low TOC content (Jiao et al., 2020). This is consistent with the different TOC content between the TMC and the underlying and overlaying TM (Table 1). Furthermore, isotopic values of the well-developed dolomite in the Lucaogou Formation suggest the significant presence of mantle-originated hydrothermal fluids (Liu et al., 2012; Jiao et al., 2020). Many other researchers also found that volcanic-hydrothermal activities may have significantly influenced hydrocarbon accumulation in the Lucaogou Formation (Pan et al., 2020; Liu et al., 2020; Zhang et al., 2021). Hence, the above characteristics serve as evidence that the volcanic-hydrothermal activities probably also played a significant role in hydrocarbon generation. However, further work needs to find some direct evidence. The characteristics of mantle-derived hydrothermal calcite grains and its hydrocarbon inclusions with a variable maturity in this study provide a direct example for the link between volcanichydrothermal activities and hydrocarbon generation.

5.5. Depositional model of tuffaceous mudstone containing sand-sized calcite grains

A depositional model of a volcanic-hydrothermal system is developed to describe the forming processes of the TMC and its hydrocarbon generation (Fig. 13A). The mudstone was deposited in a subaqueous hydrothermal system in an intracontinental lake with an anoxic and saline bottom water. Continuously-supplied hydrothermal fluid originated from the mantle had abundant calcium and methane-hydrogen gas to precipitate carbonate-rich laminae. The laminae were gradually altered and recrystallized to mono- and polycrystalline calcite (Kelley et al., 2001, 2005). During this period, hydrocarbons similar to the “hydrothermal petroleum” of Simoneit (1984); Simoneit et al. (2000) migrated from mantle directly and/ or underlying stratum and may have been formed by inorganic materials through the Fischer-Tropsch process. The hydrocarbons were incorporated into the calcite crystals. The local high temperature caused the hydrocarbon to have a high degree of maturity (Fig. 6) and to form the rhombic primary fluid-gas and hydrocarbon-rich inclusions in the calcite grains (Figs. 4, 5).

Subaqueous volcanic eruption and related hydrothermal exhalation formed two types of fragments. When a hot magma came in contact with lake water, intense fragmentation would occur to form very fine particles by fracturing the crystals in the magma (Kokelaar and Busby, 1992). However, the subaqueous volcanic eruptions were instantaneous and frequent and only produced a small amount of pyroclastics due to the hydraulic pressure of lake water (White, 2000), which occurred locally to provide feldspar-rich pyroclastic sediments. In the meanwhile, continuously upwelling hydrothermal fluid would induce increasing pressure to break through the overburden pressure of the previously formed laminated precipitates. Fragments of water bursting brecciation (Zheng et al., 2006) occurred. Comparing with the volcanic eruption, the hydrothermal brecciation is relatively weak. Fragmentation only occurs along the weak boundaries which are vertical to the grain surfaces, such as the crystal boundaries and cleavage of the calcite crystals. Hence, the calcite grains have a similar width but a variable length with smooth edges along the long axis and angular saw-toothed edges along the short axis (Fig. 2A–H). This hydrothermal exhalation fragmented the calcite laminae into mono- and poly-crystalline calcite grains with abundant micro-cracks (Fig. 2B). Both the claysized pyroclastic and the calcite grains of variable sizes were thoroughly mixed during the formation and transport of debris flows on the lake floor. Due to the high density of the flow, the deposits are overall massive. Calcite and pyroclastic grains are poorly sorted and angular. As a result of a varying degree of fragmentation of the calcite laminae, the size and content of the calcite grains are variable in the debris flow deposit (Fig. 13B). The largest grains are mainly poly-crystalline and were accumulated at the lower part of the sediments and show a crude orientation (Figs. 2A, 13B) due to depositional shear sorting (Stow, 2005). In the middle part, calcite grains are smaller and mixed with mono- and poly-crystalline calcite grains. In the upper part, the content of calcite grains gradually decreases upward (Fig. 2A). Furthermore, a large nutrition influx supplied by volcanic-hydrothermal activities induced algae blooms to promote the production of microorganisms (Xie et al., 2010). In the meanwhile, thermo-metamorphic or mantle-derived carbon dioxide and thermogenic methane were released from those activities (Procesi et al., 2019), which increased the hydrocarbon accumulation. As a result, hydrocarbon is rich in the matrix of the TMC and in the irregular-shaped inclusions in the micro-cracks in the calcite grains (Fig. 4B–D). Hydrocarbons in the TMC likely have two sources, resulting in a higher TOC content than that in the underlying and overlying TM as well as the common shales in the Lucaogou Formation in the Santanghu Basin.

6. Conclusions

Detailed mineralogical, petrographic, inorganic isotopic, and organic geochemical data documented sand-size calcite grains in hydrocarbonrich tuffaceous mudstones in the middle Permian Lucaogou Formation in the Santanghu rift basin. A model of subaqueous volcanic-hydrothermal field with high-density debris flows is developed to interpret the sedimentation of the calcite grains and related hydrocarbon accumulation. In this environment, mantle-derived hydrothermal fluids formed calcite laminae by early carbonate precipitation and later alteration. Then, local volcanic eruption and continuously hydrothermal exhalation provided clay-sized pyroclastic grains and fragmented the calcite laminae into sand sized calcite grains, respectively. Those grains mixed together and were deposited as muddy sediments with sand-sized calcite grains by debris flows on the lake floor.

This work provides an analog for the relationship between volcanichydrothermal activities and hydrocarbon generation. Hydrocarbon was partly generated by algal matter that was produced by algal bloom due to the abundant nutrition supplied by volcanic-hydrothermal activities. The other hydrocarbon may be generated directly from inorganic synthesis of materials released by the volcanic-hydrothermal activities and/or have migrated from the underlying strata. Both sources of hydrocarbons jointly formed the hydrocarbon accumulation in the calcite-bearing mudstone. Volcanic-hydrothermal center and their distal deposits should be a good potential target for shale oil exploration. The results provide insights on subaqueous volcanic-hydrothermal sedimentation and related hydrocarbon generation in lacustrine fine-grained sedimentary rocks in tectonically active rift basins.

Supplementary data to this article can be found online at https://doi.org/10.1016/j.sedgeo.2022.106158.

Declaration of competing interest

The authors declare the following financial interests/personal relationships which may be considered as potential competing interests: Xin Jiao reports financial support was provided by National Science Foundation of China. Yiqun Liu reports a relationship with National Science Foundation of China that includes: funding grants.

Acknowledgements

This work was supported by a grant from the National Science Foundation of China (41802120). We thank Dan Li in China University of Petroleum for her constructive comments on sedimentary environments, Dr. Qing Cao in Xi'an Shiyou University for her help on analysis of fluid inclusions, and the Tu-Ha Bureau of PetroChina for permission and facilitation in collection of core samples and seismic data. We are grateful to Dr. Catherine Chagué, Editor-in-Chief and two anonymous reviewers for insightful comments and suggestions that have significantly improved the manuscript.

References

Adachi, M., Yamamoto, K., Sugisaki, R., 1986. Hydrothermal chert and associated siliceous rocks from the northern Pacific: their geological significance as indication of ocean ridge activity. Sedimentary Geology 47, 125–148.

Benison, K., 2017. Gypsum gravel devils in Chile: movement of largest natural grains by wind? Geology 45, 423–426.

Benison, K., 2019. The physical and chemical sedimentology of two high-altitude acid salars in Chile: sedimentary processes in an extreme environment. Journal of Sedimentary Research 89, 147–167.

Berndt, C., Sarkar, S., Geilert, S., Schmidt, M., Liebetrau, V., Kipfer, R., Scholz, F., Doll, M., Muff, S., Karstens, J., Planke, S., Petersen, S., Böttner, C., Chi, W.C., Moser, M., Behrendt, R., Fiskal, A., Lever, M.A., Su, C.C., Deng, L., Brennwald, M.S., Lizarralde, D., 2016. Rifting under steam - how rift magmatism triggers methane venting from sedimentary basins. Geology 44, 767–770.

Bigi, S., Beaubien, G., Ciotoli, S., D'Ambrogi, C., Doglioni, C., Ferrante, V., Lombardi, S., Milli, S., Orlando, L., Ruggiero, L., Tartarello, M.C., Sacco, P., 2015. Mantle-derived CO2 migration along active faults within an extensional basin margin (Fiumicino, Rome, Italy). Tectonophysics 637, 137–149.

Boni, M., Parentea, G., Bechstadtb, T., 2000. Hydrothermal dolomites in SW Sanlinia (Italy): evidence for a widespread late-Variscan fluid flow event. Sedimentary Geology 131, 181–200.

Botz, R., Wehner, H., Schmitt, M., Worthington, T.J., Schmidt, M., Stoffers, P., 2002. Thermogenic hydrocarbons from the offshore Calypso hydrothermal field, Bay of Plenty, New Zealand. Chemical Geology 186, 235–248.

Bua, M., 1991. Rare-earth element mobility during hydrothermal and metamorphic fluidrock interaction and the significance of the oxidation state of europium. Chemical Geology 93, 219–230.

Burke, W.H., Denison, R.E., Hetherington, E.A., 1982. Variation of seawater $^{87}Sr/^{86}Sr$ throughout Phanerozoic time. Geology 10, 516–519.

Cangemi, M., Censi, P., Reimer, A., D'Alessandro, W., Hause-Reitner, D., Madonia, P., Oliveri, Y., Pecoraino, G., Reitner, J., 2016. Carbonate precipitation in the alkaline lake Specchio di Venere (Pantelleria Island, Italy) and the possible role of microbial mats. Applied Geochemistry 67, 168–176.

Cao, J., Xia, L., Wang, T., Zhi, D., Tang, Y., Li, W., 2020. An alkaline lake in the Late Paleozoic Ice Age (LPIA): a review and new insights into paleoenvironment and petroleum geology. Earth-Science Reviews 202, 103091.

Capaccioni, B., Taran, Y., Tassi, F., Vaselli, O., Mangani, G., Macias, J.L., 2004. Source conditions and degradation processes of light hydrocarbons in volcanic gases: an example from El Chichon volcano (Chiapas State, Mexico). Chemical Geology 206, 81–96.

Ciotoli, G., Etiope, G., Florindo, F., Marra, F., Ruggiero, L., Sauer, P.E., 2013. Sudden deep gas eruption nearby Rome′s airport of Fiumicino. Geophysical Research Letters 40, 5632–5636.

Connan, J., Cassou, A.M., 1980. Properties of gases and petroleum liquids derived from terrestrial kerogen at various maturation levels. Geochimica et Cosmochimica Acta 44, 1–23.

Dai, J., Yang, S., Chen, H., Shen, X., 2005. Geochemistry and occurrence of inorganic gas accumulations in Chinese sedimentary basins. Organic Geochemistry 36, 1664–1688.

Davies, G.R., Smith, L.B., 2006. Structurally controlled hydrothermal dolomite reservoir facies: an overview. AAPG 90 (11), 1641–1690.

de Silva, S.L., Spagnuolo, M.G., Bridges, N.T., Zimbelman, J.R., 2013. Gravel-mantled megaripples of the Argentinean Puna: a model for their origin and growth with implications for Mars. GSA Bulletin 125, 1912–1929.

Didyk, B.M., Simoneit, B.R.T., Brassell, S.C., Eglinton, G., 1978. Organic geochemical indicator of palaeoenvironmental conditions of sedimentation. Nature 272, 216–222.

Farhaduzzaman, M., Abdullah, W.H., Islam, M.A., 2012. Depositional environment and hydrocarbon source potential of the Permian Gondwana coals from the Barapukuria Basin, Northwest Bangladesh. International Journal of Coal Geology 90-91, 162–179.

Faure, G.P., 1986. Les of Isotope Geology. 2nd ed. John Wiley and Sons, New York, pp. 160–230.

Fischer, W.W., Knoll, A.H.I., 2009. An iron shuttle for deepwater silica in Late Archean and early Plaeoproterozoic iron formation. GSA Bulletin 121 (1–2), 222–235.

Garcia-Fresca, B., Pinkston, Daniel, Loucks, R.G., LeFever, R., 2018. The Three Forks playa lake depositional model: Implications for characterization and development of an unconventional carbonate play. AAPG Bulletin 102 (8), 1455–1488.

Genna, D., Gaboury, D., Roy, G., 2014. Evolution of a volcanogenic hydrothermal system recorded by the behavior of LREE and Eu: case study of the Key Tuffite at Bracemac–McLeod deposits, Matagami, Canada. Ore Geology Reviews 63, 160–177. Gill, R., 2010. Igneous Rocks and Processes. Wiley-Blackwell, Malaysia, p. 209 (240pp.).

Guo, P., Wen, H., Gibert, L., Jin, J., Wang, J., Lei, H., 2021. Deposition and diagenesis of the Early Permian volcanic-related alkaline playa-lake dolomitic shales, NW Junggar Basin, NW China. Marine and Petroleum Geology 123, 104780.

Hackley, P., Fishman, N., Wu, T., Baugher, G., 2016. Organic petrology and geochemistry of mudrocks from the lacustrine Lucaogou Formation, Santanghu Basin, northwest China: application to lake basin evolution. International Journal of Coal Geology 168, 20–34.

Hao, F., Zhou, X., Zhu, Y., Yang, Y., 2011. Lacustrine source rock deposition in response to co-evolution of environments and organisms controlled by tectonic subsidence and climate, Bohai Bay Basin, China. Organic Geochemistry 42 (4), 323–339.

Huang, W.Y., Meinschein, W.G., 1979. Sterols as ecological indicators. Geochimica et Cosmochimica Acta 43 (5), 739–745.

Hyatt, J.A., 1984. Liquid and supercritical carbon dioxide as organic solvents. Journal of Organic Chemistry 49, 5097–5101.

Jarvie, D.M., Claxton, B.L., Henk, F., Breyer, J.T., 2001. Oil and Shale Gas from the Barnett Shale, Fort Worth Basin, Texas. American Association of Petroleum Geologists Annual Meeting Program 10, A100.

Jiang, Z., Kong, X., Yang, Y., Zhang, J., Zhang, Y., Wang, L., Yuan, X., 2021. Multi-source genesis of continental carbonate-rich fine-grained sedimentary rocks and hydrocarbon sweet spots. Petroleum Exploration and Development 48 (1), 30–42.

Jiao, X., Liu, Y., Yang, W., Zhou, D., Li, H., Jin, M., 2018a. A magmatic-hydrothermal lacustrine exhalite from the Permian Lucaogou Formation, Santanghu Basin, NW Chinathe volcanogenic origin of fine-grained clastic sedimentary rocks. Journal of Asian Earth Sciences 156, 11–25.

Jiao, X., Liu, Y., Yang, W., Zhou, D., Wang, S., Jin, M., Sun, B., Fan, T., 2018b. Mixed biogenic and hydrothermal quartz in Permian lacustrine shale of Santanghu Basin, NW

Chinaimplications for penecontemporaneous transformation of silica minerals. International Journal of Earth Sciences 107, 1989–2009.

Jiao, X., Liu, Y., Yang, W., Zhou, D., Bai, B., Zhang, T., Zhao, M., Li, Z., Meng, Z., Yang, Y., Li, Z., 2020. Fine-grained volcanic-hydrothermal sedimentary rocks in Permian Lucaogou Formation, Santanghu Basin, NW China: implications on hydrocarbon source rocks and accumulation in lacustrine rift basins. Marine and Petroleum Geology 114, 104201.

Kelley, D.S., Karson, J.A., Blackman, D.K., Früh-Green, G.L., Butterfield, D.A., Lilley, M.D., Olson, E.J., Schrenk, M.O., Roe, K.R., Lebon, G.T., Rivizzigno, P., the AT3-60 Shipboard Party, 2001. An off-axis hydrothermal vent field near the Mid-Atlantic Ridge at 30° N. Nature 412, 145–149.

Kelley, D.S., Karson, J.A., Früh-Green, G.L., Yoerger, D.R., Shank, T.M., Butterfield, D.A., Hayes, J.M., Schrenk, M.O., Olson, E.J., Proskurowski, G., Jakuba, M., Bradley, A., Larson, B., Ludwig, K., Glickson, D., Buckman, K., Bradley, A.S., Brazelton, W.J., Roe, K., Elend, M.J., Delacour, A., Bernasconi, S.M., Lilley, M.D., Baross, J.A., Summons, R.E., Sylva, S.P., 2005. A serpentinite-hosted submarine ecosystem: the Lost City Hydrothermal Field. Science 307, 1428–1434.

Kirkbride, M.P., Winkler, S., 2012. Correlation of Late Quaternary moraines: impact of climate variability, glacier response, and chronological resolution. Quaternary Science Reviews 46, 1–29.

Kokelaar, B.P., Busby, C.J., 1992. Subaqueous explosive eruption and welding of pyroclastic deposits. Science 257, 196–201.

Langford, F.F., Blanc-Valleron, M.M., 1990. Interpreting Rock-Eval pyrolysis data using graphs of pyrolizable hydrocarbons vs. total organic carbon. AAPG Bulletin 74, 799–804.

Łapcik, P., Ninard, K., Uchman, A., 2021. Extra-large grains in Late Glacial – Early Holocene aeolian inland dune deposits of cold climate, European Sand Belt, Poland: an evidence of hurricane-speed frontal winds. Sedimentary Geology 415, 105847.

Lee, C.T.A., Jiang, H., Ronay, E., Minisini, D., Stiles, J., Neal, M., 2018. Volcanic ash as a driver of enhanced organic carbon burial in the Cretaceous. Scientific Reports 8, 4197.

Li, X., Ma, Q., Liang, H., Zhang, P., Zhang, Q., Jia, X., Pu, Z., Yan, L., Meng, Y., 2015. Geological characteristics and exploration potential of diamictite tight oil in the second Member of the Permian Lucaogou Formation, Santanghu Basin, NW China. Petroleum Exploration and Development 42 (6), 833–843.

Li, D., Li, R., Zhu, Z., Wu, X., Cheng, J., Liu, F., Zhao, B., 2017. Origin of organic matter and paleo-sedimentary environment reconstruction of the Triassic oil shale in Tongchuan City, southern Ordos Basin (China). Fuel 208, 223–235.

Liang, C., Jiang, Z., Cao, Y., Wu, J., Wang, Y., Hao, F., 2018. Sedimentary characteristics and origin of lacustrine organic-rich shales in the salinized Eocene Dongying Depression. GSA Bulletin 130 (1/2), 154–174.

Liang, S., Luo, Q., Wang, R., Chen, X., Yang, B., Ma, Q., Liang, H., 2019. Geological characteristics and exploration practice of unconventional Permian oil resources in the Santanghu Basin. China Petroleum Exploration 24 (5), 624–635 (in Chinese with English abstract).

Liu, K.Y., Eadington, 2005. Quantitative fluorescence techniques for detecting residual oils and reconstructing hydrocarbon charge history. Organic Geochemistry 36, 1023–1036.

Liu, C.L., Zhao, Q.H., Wang, P.X., 2001. Correlation between carbon and oxygen isotopic ratios of lacustrine carbonates and types of oil-producing paleolakes. Geochimica 363–367.

Liu, Y., Jiao, X., Li, H., Yuan, M., Yang, W., Zhou, X., Liang, H., Zhou, D., Zheng, C., Sun, Q., Wang, S., 2012. Mantle exhalative hydrothermal original dolostones of Permian, in Yuejingou section, Santanghu area, Xinjiang province. Science China: Earth Sciences 55, 183–192.

Liu, B., Bechtel, A., Sachsenhofer, R.F., Gross, D., Gratzer, R., Chen, X., 2017. Depositional environment of oil shale within the second member of Permian Lucaogou Formation in the Santanghu Basin, Northwest China. International Journal of Coal Geology 175, 10–25.

Liu, Q., Zhu, D., Meng, Q., Liu, J., Wu, X., Zhou, B., Fu, Q., Jin, Z., 2019. The scientific connotation of oil and gas formations under deep fluids and organic-inorganic interaction. Science China Earth Sciences 62, 507–528.

Liu, B., Song, Y., Zhu, K., Su, P., Ye, X., Zhao, W., 2020. Mineralogy and element geochemistry of salinized lacustrine organic-rich shale in the Middle Permian Santanghu Basin: Implications for paleoenvironment, provenance, tectonic setting and shale oil potential. Marine and Petroleum Geology 120, 104569.

Lonnee, J., Machel, H.G., 2006. Pervasive dolomitization with subsequent hydrothermal alteration in the Clarke Lake gas field, Middle Devonian Slave Point Formation, British Columbia, Canada. AAPG Bulletin 90 (11), 1739–1761.

Mackenzie, A.S., Brassell, S.C., Eglinton, G., Maxwell, J.R., 1982. Chemical fossils: the geological fate of steroids. Science 217, 491–504.

Ma, L., Qiao, X., Min, L., Fan, B., 2002. Geological Atlas of China: Beijing. Geological Publishing House in Chinese.

Mazzullo, S.J., 2000. Organogenic dolomitization in peritidal to deep-sea sediments. Journal of Sedimentary Research 70 (1), 10–23.

Michaelis, W., Jenisch, A., Richnow, H.H., 1990. Hydrothermal petroleum generation in Red Sea sediments from the Kebrit and Shaban Deeps. Applied Geochemistry 5, 103–114.

Mulder, T., Alexander, J., 2001. The physical character of subaqueous sedimentary density flows and their deposits. Sedimentology 48 (2), 269–299.

Newell, D.L., Jensen, J.L., Frantz, C.M., Vanden Berg, M.D., 2017. Great Salt Lake (Utah) microbialite δ13C, δ18O, and δ15N record fluctuations in lake biogeochemistry since the late Pleistocene. Geochemistry, Geophysics, Geosystems 18, 3631–3645.

Palmer, M.R., Elderfield, H., 1985. Sr isotope composition of sea water over the past 75 Myr. Nature 314, 526–528.

Pan, Y., Huang, Z., Li, T., Guo, X., Xu, X., Chen, X., 2020. Environmental response to volcanic activity and its effect on organic matter enrichment in the Permian Lucaogou Formation of the Malang Sag, Santanghu Basin, Northwest China. Palaeogeography, Palaeoclimatology, Palaeoecology 560, 110024.

Procesi, M., Ciotoli, G., Mazzini, A., Etiope, G., 2019. Sediment-hosted geothermal systems: review and first global mapping. Earth-Science Reviews 192, 529–544.

Riboulleau, A., Schnyder, J., Riquier, L., Lefebvre, V., Baudin, F., Deconinck, J.F., 2007. Environmental change during the Early Cretaceous in the Purbeck-type Durlston Bay section (Dorset, Southern England): A biomarker approach. Organic Geochemistry 38, 1804–1823.

Ryder, A.G., 2005. Analysis of Crude Petroleum Oils Using Fluorescence Spectroscopy. In: Geddes, C.D., Lakowicz, J.R. (Eds.), Reviews in Fluorescence 2005. Reviews in Fluorescencevol 2005. Springer, Boston, MA.

Shan, X., Li, J., Chen, S., Ran, Q., Chen, G., Liu, C., 2013. Subaquatic volcanic eruptions in continental facies and their influence on high quality source rocks shown by the volcanic rocks of a faulted depression in Northeast China. Science China: Earth Sciences 56, 1926–1933.

Shuai, Y., Etiope, G., Zhang, S., Douglas, P.M.J., Huang, L., Eiler, J.M., 2018. Methane clumped isotopes in the Songliao Basin (China): new insights into abiotic vs. biotic hydrocarbon formation. Earth and Planetary Science Letters 482, 213–221.

Si, S.H., Zhao, J.Z., Zou, G.L., Li, J., Meng, X.N., Liu, C., 2020. Relationship between aromatic component types and maturity in crude oil inclusions: a case study of Fuyu reservoir in Sanzhao Sag. Acta Petrologica Sinica 41 (7), 835–864 (in Chinese with English abstract).

Siever, R., 1962. Silica solubility, 0-200 °C., and the diagenesis of siliceous sediments. The Journal of Geology 70 (2), 127–150.

Simoneit, B.R.T., 1984. Hydrothermal effects on organic matter-High vs low temperature components. Organic Geochemistry 6, 857–864.

Simoneit, B.R.T., Aboul-Kassim, T.A.T., Tiercelin, J.J., 2000. Hydrothermal petroleum from lacustrine sedimentary organic matter in the East African Rift. Applied Geochemistry 15, 355–368.

Smith, L.B., 2006. Origin and reservoir characteristics of Upper Ordovician Trenton-Black Rivers in New York. AAPG Bulletin 90 (11), 1691–1718.

Stow, A.V.D., 2005. Sedimentary Rocks in the Field, A color guide. CRC Press (42pp.).

Sun, S.-S., McDonough, W.F., 1989. Chemical and isotopic systematics of oceanic basalts: implications for mantle composition and processes. Geological Society London Special Publications 42, 313–345.

Talbot, M.R., Kelts, K., 1990. Paleolimnological signatures from carbon and oxygen isotopic ratios in carbonates from organic carbon-rich lacustrine sediments. AAPG Bulletin 50, 99–112.

Volkman, J.K., 1986. A review of sterol markers for marine and terrigenous organic matter. Organic Geochemistry 9 (2), 83–99.

Wacey, D., Wright, D.T., Boyce, A.J., 2007. A stable isotope study of microbial dolomite formation in the Coorong Region, South Australia. Chemical Geology 244, 155–174.

Wang, S., Liu, Y., Zhang, H., Zhou, D., Jiao, X., Nan, Y., 2015. Geochemical characteristics and tectonic setting of the Middle Permian Tiaohu Formation mafic-ultramafic rocks of Santanghu area, Xinjiang, Northwest China. Science China: Earth Sciences 58, 1924–1938.

Weitze, W.Z., 1985. New aspects on the formation of hydrocarbon source rocks. Geologische Rundschau 74 (2), 385–416.

Wen, H., Zheng, R., Qing, H., Fan, M., Li, Y., Gong, B., 2013. Primary dolostone related to the Cretaceous lacustrine hydrothermal sedimentation in Qingxi Sag, Jiuquan Basin on the northern Tibetan Plateau. Science China: Earth Sciences 56, 2080–2093.

Westoby, M.J., Glasser, N.F., Brasington, J., Hambrey, M.J., Quincey, D.J., Reynolds, J.M., 2014. Modelling outburst floods from moraine-dammed glacial lakes. Earth-Science Reviews 134, 137–159.

White, J.D.L., 2000. Subaqueous eruption-fed density currents and their deposits. Precambrian Research 101, 87–109.

White, J.D.L., Houghton, B.F., 2006. Primary volcaniclastic rocks. Geology 34 (8), 677–680.

Williams, L.A., Crerar, D.A., 1985. Silica diagenesis, II. General mechanisms. Journal of Sedimentary Petrology 55 (3), 312–321.

Wright, V.P., 2012. Lacustrine carbonates in rift settings: the interaction of volcanic and microbial processes on carbonate deposition. Geological Society London Special Publications 370 (1), 39–47.

Xia, L., Xia, Z., Xu, X., Li, X., Ma, Z., 2008. Petrogenesis of Carboniferous-Early Permian riftrelated volcanic rocks in the Tianshan and its neighboring areas, Northwestern China. Northwestern Geology 41 (4), 1–68 (in Chinese).

Xie, S., Pancost, D.R., Wang, Y., Yang, H., Wignall, B.P., Luo, G., Jia, C., Chen, L., 2010. Cyanobacterial blooms tied to volcanism during the 5 m.y. Permo-Triassic biotic crisis. Geology 38 (5), 447–450.

Xu, X., Yi, C., 2014. Little Ice Age on the Tibetan Plateau and its bordering mountains: evidence from moraine chronologies. Global and Planetary Change 116, 41–53.

Xu, X., Yu, X., Qing, Z., Zhang, Y., Li, T., Yu, H., Wang, B., 2020. Lithofacies characteristics and its relationship with shale oil reservoirs of Lucaogou Formation in Santanghu Basin. Xinjiang Petroleum Geology 41 (6), 677–684 (in Chinese with English abstract).

Yang, W., Liu, Y., Feng, Q., Lin, J., Zhou, D., Wang, D., 2007. Sedimentary evidence of earlylate Permian mid-latitude continental climate variability, southern Bogda Mountains, NW China. Palaeogeography, Palaeoclimatology, Palaeoecology 252, 239–258.

Yang, W., Feng, Q., Liu, Y., Tabor, N., Miggins, D., Crowley, J.L., Lin, J., Thomas, S., 2010. Depositional environments and cyclo- and chronostratigraphy of uppermost Carboniferous-Lower Triassic fluvial-lacustrine deposits, southern Bogda Mountains, NW China-a terrestrial paleoclimatic record of mid-latitude NE Pangea. Global and Planetary Change 73 (1–2), 15–113.

Yang, Z., Zhong, D., Whitaker, F., Lu, Z., Zhang, S., Tang, Z., Liu, R., Li, Z., 2020. Synsedimentary hydrothermal dolomites in a lacustrine rift basin: petrographic and geochemical evidence from the lower Cretaceous Erlian Basin, Northern China. Sedimentology 67 (1), 305–329.

Yang, W., Wan, M., Crowley, J.L., Wang, J., Luo, X., Tabor, N., Angielczyk, K.D., Gastaldo, R., Geissman, J., Liu, F., Roopnarine, P., Sidor, C.A., 2021b. Paleoenvironmental and paleoclimatic evolution and cyclo- and chrono-stratigraphy of upper Permian-Lower Triassic fluvial-lacustrine deposits in Bogda Mountains, NW China – Implications for diachronous plant evolution across the Permian Triassic boundary. Earth-Science Reviews 222, 103741.

Yang, Z., Zhong, D., Whitaker, F., Sun, H., Su, C., Cao, X., 2021a. Reservoir quality of tight oil plays in lacustrine rift basins: Insights from early cretaceous fine-grained hydrothermal dolomites of the Erlian Basin, NE China. Marine and Petroleum Geology 124, 104827.

Zhang, S., Liu, C., Liang, H., Wang, J., Bai, J., Yang, M., Liu, G., Huang, H., Guan, Y., 2018. Paleoenvironmental conditions, organic matter accumulation, and unconventional hydrocarbon potential for the Permian Lucaogou Formation organic-rich rocks in Santanghu Basin, NW China. International Journal of Coal Geology 185, 44–60.

Zhang, K., Liu, R., Liu, Z., Li, L., Wu, X., Zhao, K., 2020. Influence of paleoclimate and hydrothermal activity on organic matter accumulation in lacustrine black shales from the Lower Cretaceous Bayingebi Formation of the Yin′e Basin, China. Palaeogeography, Palaeoclimatology, Palaeoecology 560, 110007.

Zhang, S., Liu, C., Liang, H., Jia, L., Bai, J., Zhang, L., Wang, J., 2021. Mineralogical composition and organic matter characteristics of lacustrine fine-grained volcanichydrothermal sedimentary rocks: a data-driven analytics for the second member of Permian Lucaogou Formation, Santanghu Basin, NW China. Marine and Petroleum Geology 126, 104920.

Zheng, R., Wen, H., Fan, M., Wang, M., Xia, P., 2006. Lithological characteristics of sublacustrine white smoke type exhalative rock of the Xiagou Formation in Jiuxi Basin. Acta Petrologica Sinica 22 (12), 3027–3038.

Zhou, D., Liu, Y., Xing, X., Hao, J., Dong, Y., Ouyang, Z., 2006. The paleotectonic setting reverting and regional tectonic setting tracking of basalt during Permian in Tu-Ha, Santanghu basin in Xinjiang. Science in China Series D: Earth Sciences 36 (2), 143–153 (in Chinese).

Zhu, J., Li, S., Sun, X., Zhu, J., Xin, M., Xu, H., 1994. Discovery of early tertiary hydrothermal activity and its significance in oil/gas geology, Dongpu Depression, Henan Province, China. Chinese Journal of Geochemistry 13, 270–283.

Zou, C., Yang, Z., Zhang, G., Hou, L., Zhu, R., Tao, S., Yuan, X., Dong, D., Wang, Y., Guo, Q., Wang, L., Bi, H., Li, D., Wu, N., 2014. Conventional and unconventional petroleum "orderly accumulation": concept and practical significance. Petroleum Exploration and Development 41, 14–30.

Zhu, S., Yue, H., Zhu, X., Sun, S., Wei, W., Liu, X., Jia, Y., 2017. Dolomitization of Felsic volcaniclastic rocks in continental strata: A study from the Lower Cretaceous of the A′nan Sag in Er′lia Basin, China. Sedimentary Geology 353, 13–27.